MOX-Report No. 51/2015

Fast simulations of patient-specific haemodynamics of coronary artery bypass grafts based on a POD–Galerkin method and a vascular shape parametrization

Ballarin, F.; Faggiano, E.; Ippolito, S.; Manzoni, A.; Quarteroni, A.; Rozza, G.; Scrofani, R.

MOX, Dipartimento di Matematica
Politecnico di Milano, Via Bonardi 9 - 20133 Milano (Italy)

mox-dmat@polimi.it http://mox.polimi.it

FAST SIMULATIONS OF PATIENT-SPECIFIC HAEMODYNAMICS OF CORONARY ARTERY BYPASS GRAFTS BASED ON A POD–GALERKIN METHOD AND A VASCULAR SHAPE PARAMETRIZATION

FRANCESCO BALLARIN[a,1], ELENA FAGGIANO[a,2], SONIA IPPOLITO[b], ANDREA MANZONI[c], ALFIO QUARTERONI[a,c,3], GIANLUIGI ROZZA[d], AND ROBERTO SCROFANI[e]

Abstract. In this work a *reduced-order computational framework* for the study of haemodynamics in three-dimensional *patient-specific* configurations of coronary artery bypass grafts dealing with a wide range of scenarios is proposed. We combine several efficient algorithms to face at the same time both the geometrical complexity involved in the description of the vascular network and the huge computational cost entailed by time dependent patient-specific flow simulations. Medical imaging procedures allow to reconstruct patient-specific configurations from clinical data. A *centerlines-based parametrization* is proposed to efficiently handle geometrical variations. *POD–Galerkin reduced-order models* are employed to cut down large computational costs. This computational framework allows to characterize blood flows for different physical and geometrical variations relevant in the clinical practice, such as stenosis factors and anastomosis variations, in a rapid and reliable way. Several numerical results are discussed, highlighting the computational performance of the proposed framework, as well as its capability to perform sensitivity analysis studies, so far out of reach.

1. Introduction and motivation

Coronary artery disease represents one of the leading causes of mortality worldwide. Coronary arteries supply oxygenated blood to the heart, and the occlusion of one or more major coronary arteries may lead to angina pectoris, heart attack and heart failure. *Coronary artery bypass grafting* is a surgical procedure to restore sufficient blood flow to the heart, creating new paths around narrowed coronary arteries [1].

Clinical experience suggests that coronary artery bypass grafts (CABGs) tend to fail some years after the surgery due to the development of intimal thickening or restenosis. In fact, even though early graft failure (within thirty days) might be related to possible surgical technical errors and thrombosis, late graft failures are caused by progression of atherosclerosis and intimal hyperplasia [1, 2]. In this respect, simulating blood flow dynamics in bypass grafts configurations may provide a valuable tool in view of improving prosthetic devices such as CABGs. Indeed, altered or unfavorable flow conditions near the anastomosis (that is, the junction between the graft and the host artery) trigger the genesis and development of intimal thickening [3, 4] in locations like distal anastomosis and the coronary artery wall near the anastomosis [5, 6].

[a]MOX - Modeling and Scientific Computing, Dipartimento di Matematica, Politecnico di Milano, P.za Leonardo da Vinci 32, I-20133 Milano, Italy.

[b]Radiology Unit, Ospedale Luigi Sacco, Via G. B. Grassi 74, I-20157 Milano, Italy.

[c]CMCS - Modelling and Scientific Computing, Ecole Polytechnique Fédérale de Lausanne, Station 8, CH-1015 Lausanne, Switzerland.

[d]mathLab, Mathematics Area, SISSA, International School for Advanced Studies, via Bonomea 265, I-34136 Trieste, Italy.

[e]Cardiovascular Surgery Unit, Ospedale Luigi Sacco, Via G. B. Grassi 74, I-20157 Milano, Italy.

[1]Current address: mathLab, Mathematics Area, SISSA, International School for Advanced Studies, via Bonomea 265, I-34136 Trieste, Italy.

[2]Current address: Computational Mechanics & Advanced Materials Group, Department of Civil Engineering and Architecture, University of Pavia, via Ferrata 3, I-27100 Pavia, Italy.

[3]Currently on leave from MOX, Politecnico di Milano.

Even though clinical imaging, such as Magnetic Resonance Imaging (MRI) and Doppler ultrasound techniques, can be used to provide a noninvasive quantification of flow indices (see e.g. the review in [7]), an increasing interest in the medical and surgical community has been oriented to the development of computational methods for cardiovascular applications (see e.g. [8] and references therein). In this regard, the use of medical imaging allows to obtain *patient-specific* geometrical configurations and nowadays stands at the basis of numerical simulations. Classical computational methods, such as the finite element method, currently enable to explore a huge variety of cases (possibly depending on different *parameters* of interest) that are not readily available in vivo. However, one of their main drawback is the large computational time required for each simulation. In particular, whenever interested in exploring a wide variation of flow conditions and/or geometrical features on a complex, three dimensional configuration, the solution of a finite element problem for *each* new physical or geometrical scenario is usually very expensive and, in some cases (e.g. for sensitivity analyses or optimization, related for instance to the clinical question of sensitivity of the surgery to different stenosis entities or graft configurations), unaffordable.

The main goal of this work is to propose a *reduced-order framework* capable of handling patient-specific clinical data using a wealth of computational reduction techniques. The clinical problem at hand will be therefore cast into a suitable parametrized framework, and the combination of shape parametrization and reduced-order models (ROMs) will then be applied to cut down large computational costs [9]. The main advantage over classical methods is that faster evaluations are made possible thanks to a database of representative solutions, previously computed and stored, used as basis functions. Early results on the coupling between ROMs, parametrization techniques and *idealized* CABGs configurations have been proposed in [10, 11, 12, 13, 14, 15, 16]. In this work ROMs will be applied to *patient-specific* CABGs configurations for the first time ever. Even though different methodologies of ROMs for patient-specific CFD have been applied for few other clinical problems [17, 18], CABGs feature remarkable challenges related in particular to the complex network of coronary arteries and grafts, and its possible variation in a parametric study.

Our approach is characterized by the original combination of three main features. The first one is related to *clinical data acquisition and medical imaging techniques*, that are employed to reconstruct a computational mesh from computed tomography scans of some selected cases, among patients who have recently undergone coronary artery bypass surgery at Ospedale Luigi Sacco in Milan (Section 2). The second one is related to the introduction of a *parametrized framework* capable of handling several relevant aspects by means of few parameters, concerning in particular the variation of the patient-specific geometry (Section 3). Indeed, recent reviews [19, 20, 21, 22] have highlighted the relevance of several geometrical features in the study of CABGs, such as stenosis severity or grafting angles, along with physical parameters related to boundary conditions. The third one is the application of *computational reduction techniques* for unsteady parametrized Navier-Stokes equations, based on proper orthogonal decomposition [23], in order to evaluate the haemodynamics for different flow conditions or different geometrical features in a rapid and reliable way (Section 4). Numerical results concerning the application of the whole reduced-order computational framework to several patient-specific cases will be analyzed in Section 5. Finally, Section 6 will detail some conclusions.

2. Medical imaging

The medical imaging pipeline[1] that has been employed to reconstruct patient-specific CABGs configurations is illustrated in Figure 1. We also refer to [26, Chapter 2] for more details on this topic. Both a post-surgical Computed Tomography (CT) scan[2] and a pre-surgery angiographic study by means of a coronary angiography[3] are performed. CT scan data are employed to obtain

[1]The Vascular Modelling Toolkit `vmtk` [24] and `3DSlicer` [25] are employed.

[2]A Philips Brilliance CT 64-slice system is employed to perform a contrast enhanced computed tomography scan study.

[3]A Toshiba angiography system is employed.

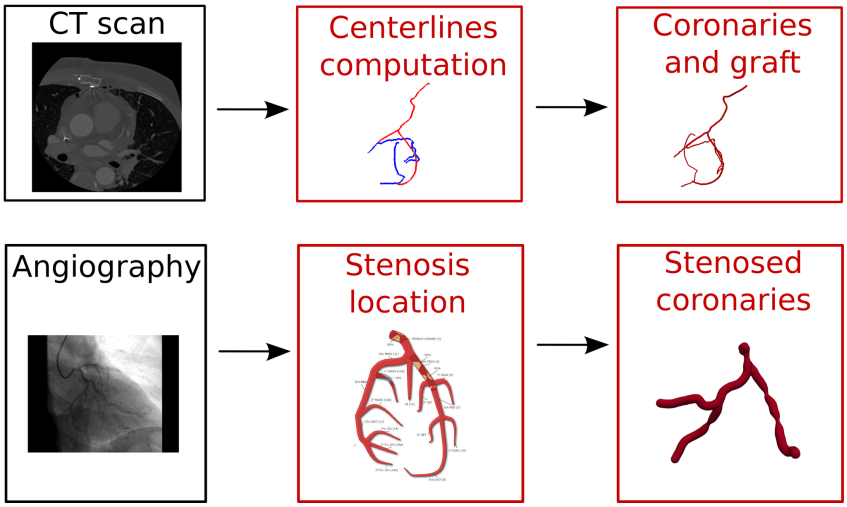

FIGURE 1. Summary of the medical imaging pipeline

a three-dimensional reconstruction of the patient-specific geometry after surgery. A level set segmentation is carried out for each patient [27, 24] to obtain a tentative geometry. Afterwards, vessel centerlines are extracted [28]. We refer to centerline as to the curve $\boldsymbol{\gamma}(s)$ drawn from the two outermost sections of the tentative geometry, which locally maximizes the distance from the vessel boundary. Moreover, the value of the maximal inscribed sphere radius $r(s)$ is associated to each centerline point. A running average smoothing on the coordinates and a linearization (with respect to the curvilinear abscissa) on the radius of the vessels have been operated, too. Afterwards, the surface corresponding to each branch of coronary arteries and bypass grafts is obtained by sweeping a circular section of variable radius $r(s)$ along each centerline $\boldsymbol{\gamma}(s)$. The resulting surface can be described as a generalized cylinder as follows:

$$\boldsymbol{B}(\rho, \varphi, s) = \boldsymbol{\gamma}(s) + \rho r(s) \left[\cos\varphi\, \boldsymbol{n}_1(s) + \sin\varphi\, \boldsymbol{n}_2(s)\right] \tag{1}$$

being $\boldsymbol{\gamma}(s)$ the centerline, (ρ, φ, s) "cylindrical" coordinates of the vessel (local radius, angle, curvilinear abscissa, respectively) and $(\boldsymbol{t}(s(\boldsymbol{x})), \boldsymbol{n}_1(s(\boldsymbol{x})), \boldsymbol{n}_2(s(\boldsymbol{x}))$ is a reference coordinate frame on the centerline. As it will be discussed in the next section, the cylindrical representation (1) will play a fundamental role in the proposed *centerlines-based parametrization*. Once the union of the surfaces corresponding to each branch has been performed, its interior is filled with volumetric elements in order to obtain a radius adaptive volume mesh. Moreover, clinical information on the native coronary artery disease (and, in particular, its location), acquired in a pre-surgery angiographic study, will be employed as well in the shape parametrization, as detailed in Section 3.1.

3. A CENTERLINES-BASED PARAMETRIZATION FOR PATIENT-SPECIFIC CABGS

In this section a vascular shape parametrization tailored for the current application is introduced, in view of the combination with computational reduction techniques. We assume that coronary arteries and bypass grafts can be represented as a network of tubular geometries and that an efficient variation of geometrical quantities of clinical interest, such as stenoses entities and anastomosis type, is required (see Figure 2). The shape parametrization that we propose allows handling the deformation of three-dimensional vessels by displacing and/or rotating few points on their unidimensional centerlines, or possibly varying the local radius. We denote by $\boldsymbol{\alpha} = [\alpha_i]_{i=1,\dots,n_S}$ and $\boldsymbol{\delta\theta} = [\delta\theta_i]_{i=1,\dots,n_G}$ the geometrical parameters we are interested in, expressing stenosis factors α_i and variation of grafting angles $\delta\theta_i$. A straightforward interpretation of such input parameters (radius, angles) and high quality deformed meshes are obtained in this way.

A partitioned approach is pursued in this work for the definition of the shape parametrization. The network is divided into n_B branches, denoted by the index $b = 1, \dots, B$, and A anastomosis/bifurcations between branches, denoted by the index $a = 1, \dots, n_A$; for instance, $n_A = 1$ and $n_B = 2$ in the network of Figure 4, where $a = 1$ corresponds to the anastomosis, highlighted in red, while $b = 1$ ($b = 2$, respectively) corresponds to branches represented in blue (respectively, green) color. A shape parametrization map (e.g. to deform the configuration in Figure 4a to the one in Figure 4b), which we will refer to as *centerlines-based parametrization*, can be defined as follows:

$$\boldsymbol{T}(\boldsymbol{x};\ \boldsymbol{\alpha},\ \boldsymbol{\delta\theta}) = \begin{cases} \boldsymbol{C}_b(\boldsymbol{x};\ \boldsymbol{\eta}'(\boldsymbol{\delta\theta}),\ \boldsymbol{\omega}(\boldsymbol{\alpha})) & b = 1, \dots, n_B, \\ \boldsymbol{V}_a(\boldsymbol{x};\ \boldsymbol{\eta}'(\boldsymbol{\delta\theta})) & a = 1, \dots, n_A, \end{cases} \tag{2}$$

where $\boldsymbol{C}_b$ is a curve-based parametrization determining the deformation of each branch and $\boldsymbol{V}_a$ is a volume-based map used to impose interface conditions between different branches. For the sake of notation, auxiliary parameters $\boldsymbol{\eta}$, $\boldsymbol{\eta}'$ and $\boldsymbol{\omega}$ have been introduced, and their meaning will be clarified in the following sections, in which we will describe the two approaches. A graphical illustration of the capability of the proposed centerlines-based parametrization (2) on a patient-specific case is provided in Figure 2.

3.1. **Curve-based parametrization of a single vessel.** Let $\boldsymbol{\gamma} : [a, b] \to \mathbb{R}^3$ be a C^2 curve in $\mathbb{R}^3$, which represents the centerline of a vessel (branch of coronary artery or bypass graft), and $r : [a, b] \to \mathbb{R}$ be the vessel radius. Curve-based approaches have been proposed in literature for general objects [29, 30, 31], as well as in cardiovascular applications [32, 28, 33]. Our approach, however, is the first one to combine curve-based and volume-based parametrizations. A parametrized description and deformation of the vessel is performed according to the following three steps, summarized in Figure 3:

(A) *Preprocessing.* A moving coordinate frame $(\boldsymbol{t}(s), \boldsymbol{n}_1(s), \boldsymbol{n}_2(s))$ attached to $\boldsymbol{\gamma}(s)$ is defined, by means of a parallel transport procedure (this procedure yields the so-called Bishop frame, see e.g. [34, 35]). Then, "cylindrical" coordinates $\rho(\boldsymbol{x}) \in [0, 1], \varphi(\boldsymbol{x}) \in [0, 2\pi), s(\boldsymbol{x}) \in [a, b]$ are obtained for each point in the vessel reference configuration as follows:

$$\begin{cases} s(\boldsymbol{x}) = \arg\min_{s\in[a,b]} \|\boldsymbol{x} - \boldsymbol{\gamma}(s)\| = \{s : [\boldsymbol{x} - \boldsymbol{\gamma}(s)] \cdot \boldsymbol{t}(s) = 0\}, \\ \varphi(\boldsymbol{x}) = \arctan\left(\frac{[\boldsymbol{x}-\boldsymbol{\gamma}(s(\boldsymbol{x}))]\cdot\boldsymbol{n}_2(s(\boldsymbol{x}))}{[\boldsymbol{x}-\boldsymbol{\gamma}(s(\boldsymbol{x}))]\cdot\boldsymbol{n}_1(s(\boldsymbol{x}))}\right), \\ \rho(\boldsymbol{x}) = \|\boldsymbol{x} - \boldsymbol{\gamma}(s(\boldsymbol{x}))\| / r(s(\boldsymbol{x})). \end{cases}$$

(B) *Deformation of the* curve *and variation of the* radius. Let $\{\boldsymbol{\eta}, \boldsymbol{\eta}', \boldsymbol{\omega}\}$ be a set of *auxiliary* geometrical parameters. We refer to $\{\boldsymbol{\eta}, \boldsymbol{\eta}', \boldsymbol{\omega}\}$ as auxiliary parameters since their value is automatically obtained from the (clinically relevant) parameters $\{\boldsymbol{\alpha}, \boldsymbol{\delta\theta}\}$, as follows:

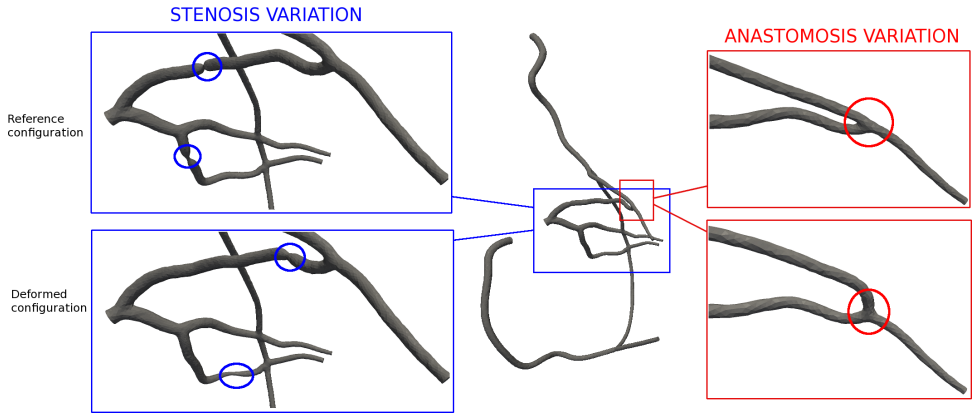

FIGURE 2. Application of the centerlines-based parametrization to a patient-specific configuration.

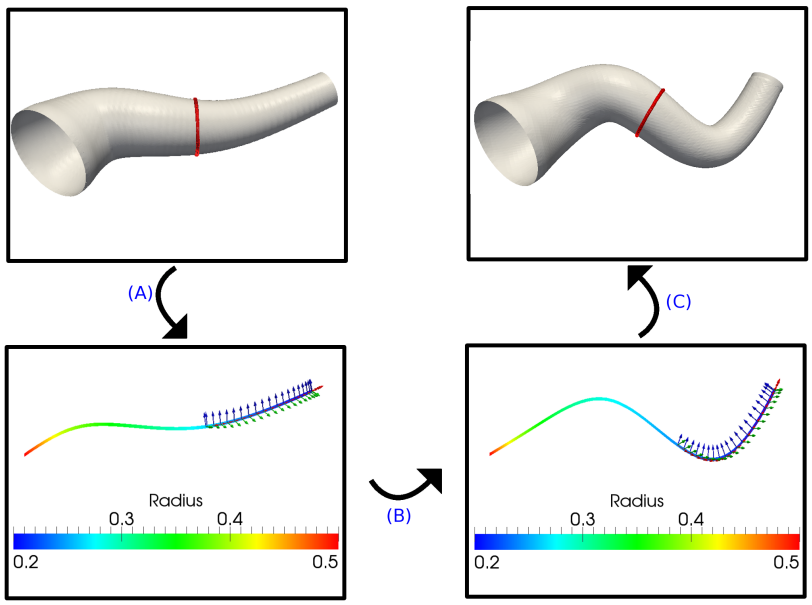

FIGURE 3. A centerline based parametrization

(B') $\boldsymbol{\eta} = \{\boldsymbol{\eta}_i \in \mathbb{R}^3\}_{i=1,\dots,N}$ is related to the displacement of a (possibly, small) number N of points located at curvilinear abscissas $\{\vartheta_i\}_{i=1,\dots,N}$ on the curve, and $\boldsymbol{\eta}' = \{\boldsymbol{\eta}'_j \in \mathbb{R}^3\}_{j=1,\dots,M}$ is the variation of the first derivative of the curve at another (possibly overlapping) set of M points at curvilinear abscissas $\{\boldsymbol{\varkappa}_j\}_{j=1,\dots,M}$. A deformed configuration $\boldsymbol{\gamma}(s;\boldsymbol{\eta},\boldsymbol{\eta}')$ of the curve is thus obtained interpolating the prescribed variations $\boldsymbol{\eta}$ and $\boldsymbol{\eta}'$; in particular we employ a radial basis functions interpolation (see A.1) because of its generality and versatility. Finally, after the deformation an updated moving coordinate frame $(\boldsymbol{t}(s;\boldsymbol{\eta},\boldsymbol{\eta}'),\ \boldsymbol{n}_1(s;\boldsymbol{\eta},\boldsymbol{\eta}'),\ \boldsymbol{n}_2(s;\boldsymbol{\eta},\boldsymbol{\eta}'))$ can be computed. We will discuss in Section 3.2 how to prescribe local variation $\boldsymbol{\eta}'$ of the tangent vector in order to parametrize different grafting angles $\boldsymbol{\delta\theta}$.

(B") Moreover, $\boldsymbol{\omega}$ is related to variation of stenoses entities $\boldsymbol{\alpha}$ and locations, and the deformed local radius is encoded in a parametrized function $r(s(\boldsymbol{x});\boldsymbol{\omega})$. For instance, in the case of a single stenosis,

$$r(s;\boldsymbol{\omega}) = r(s)\sqrt{1-\alpha\exp\left(-\frac{(s-\mu)^2}{2\sigma^2}\right)}, \quad \boldsymbol{\omega}(\alpha) = \alpha.$$

This function is used to represent a stenosis at the point located at curvilinear abscissa μ, where the factor α is the surface reduction and the standard deviation σ controls the "extension" of the stenotic region. In the following, μ and σ are quantified from the available clinical data, and α is the clinical parameter of interest related to stenosis variation. The proposed approach can be easily extended to the case of multiple stenoses $\boldsymbol{\omega} = \boldsymbol{\omega}(\boldsymbol{\alpha}) = (\alpha_1, \alpha_2, \dots, \alpha_{n_S})$, or of additional parametrizations, considering e.g. the location of the stenosis as an additional parameter $\boldsymbol{\omega} = \boldsymbol{\omega}(\alpha,\mu) = (\alpha,\mu)$.

(C) *Postprocessing: deformation of the* vessel. The *vessel* is deformed by the map $\boldsymbol{C}(\cdot;\boldsymbol{\eta},\boldsymbol{\eta}',\boldsymbol{\omega}) : \mathbb{R}^3 \to \mathbb{R}^3$,

$$\begin{aligned}\boldsymbol{C}(\boldsymbol{x};\boldsymbol{\eta},\boldsymbol{\eta}',\boldsymbol{\omega}) &= \boldsymbol{C}(\{\rho(\boldsymbol{x}),\varphi(\boldsymbol{x}),s(\boldsymbol{x})\};\boldsymbol{\eta},\boldsymbol{\eta}',\boldsymbol{\omega}) \\ &= \boldsymbol{\gamma}(s(\boldsymbol{x});\boldsymbol{\eta},\boldsymbol{\eta}') + \rho r(s(\boldsymbol{x});\boldsymbol{\omega})\left[\cos\varphi(\boldsymbol{x})\ \boldsymbol{n}_1(s(\boldsymbol{x});\boldsymbol{\eta},\boldsymbol{\eta}')\right. \\ &\quad \left. + \sin\varphi(\boldsymbol{x})\ \boldsymbol{n}_2(s(\boldsymbol{x});\boldsymbol{\eta},\boldsymbol{\eta}')\right].\end{aligned} \tag{3}$$

The resulting map $\boldsymbol{C}(\cdot;\boldsymbol{\eta},\boldsymbol{\eta}',\boldsymbol{\omega})$ thus provides the deformation of the three-dimensional vessel between a reference configuration (say, a branch of the patient-specific network) and the deformed configuration, obtained as a function of the displacements $\boldsymbol{\eta}$, variations $\boldsymbol{\eta}'$ of the tangent vector, and local radius variations $\boldsymbol{\omega}$ of the centerline.

3.2. **Volume-based parametrization of anastomosis/bifurcation regions.** The main advantage of the centerline-based parametrization proposed in the previous section is the capability to deform a three-dimensional shape acting on a unidimensional object. However, the unidimensionality assumption does not hold near bifurcations of native vessels or anastomoses of coronary arteries and bypass grafts. To this end, a volume-based parametrization (i.e. a description in which input parameters are not necessarily related to a curve, but more generally to the entire volume) is used in these regions, instead of a curve-based description. As for the curve-based case, we interpolate the deformed position of few control points, so that the regularity of the global map is ensured.

In particular, remarkable clinical interest is related to the variation of anastomosis between antegrade (same direction for graft flow and native vessel flow in the anastomosis), T-shaped (graft almost perpendicular to the native vessel) and retrograde (opposite directions for graft flow and native vessel flow in the anastomosis) cases [36, 5], which can be related to the variation $\delta\theta$ of the grafting angle. In this section we will describe the relation between $\delta\theta$ and $\boldsymbol{\eta}'$ at step (B') of the centerline-based parametrization, and how to prescribe compatibility conditions between different subdomains thanks to an additional step (D).

(B') Denoting by $\boldsymbol{t}_c$ and $\boldsymbol{t}_g$ the tangent vectors of the coronary artery and the graft in the reference configuration (blue and green subdomains in Figure 4a, respectively), the rotation of the graft of an angle $\delta\theta$ can be obtained with the following choice of $\boldsymbol{\eta}' = \boldsymbol{\eta}'(\delta\theta)$

$$\boldsymbol{k} = \frac{\boldsymbol{t}_g \times \boldsymbol{t}_c}{\|\boldsymbol{t}_g \times \boldsymbol{t}_c\|}, \quad R(\delta\theta) = I_{3\times 3} + [\boldsymbol{k}]_\times \sin\delta\theta + (1-\cos\delta\theta)[\boldsymbol{k}]_\times^2, \quad \boldsymbol{\eta}'(\delta\theta) = (R(\delta\theta) - I_{3\times 3})\boldsymbol{t}_g,$$

where $[\boldsymbol{k}]_\times \in \mathbb{R}^{3\times 3}$ denotes the cross-product matrix such that $[\boldsymbol{k}]_\times \boldsymbol{v} = \boldsymbol{k}\times\boldsymbol{v}$ for all $\boldsymbol{v}\in\mathbb{R}^3$.

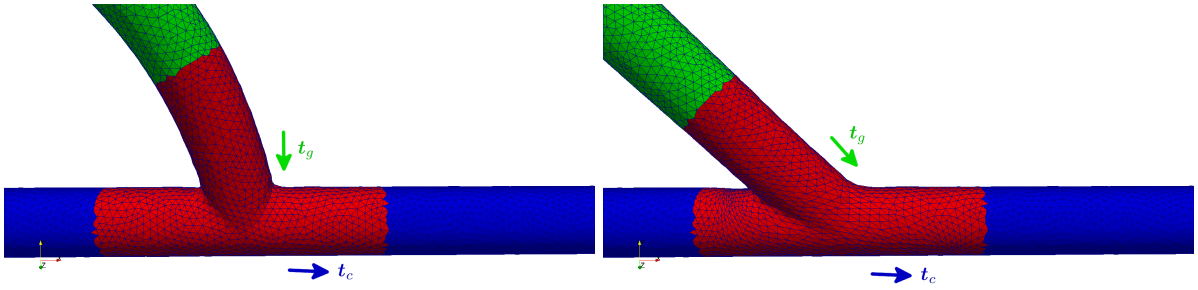

(A) T-shaped anastomosis (reference domain). (B) Antegrade anastomosis (deformed domain).

FIGURE 4. Example of anastomosis variation: the mesh of a T-shaped anastomosis (on the left) is deformed into an antegrade one (right).

(D) In this step, the deformation of the anastomosis/bifurcation (red subdomain in Figure 5a) occurs. The deformed position of L control points $\{\boldsymbol{p}_l\}_{l=1,\dots,L}$ (located not necessarily on the centerlines, but e.g. on the interface between the subdomains) is interpolated employing a volume-based parametrization $\boldsymbol{V}(\boldsymbol{x};\boldsymbol{\eta},\boldsymbol{\eta}')$, such as the one summarized in A.2. Their displacement vectors $\{\boldsymbol{d}_l(\boldsymbol{\eta},\boldsymbol{\eta}')\}_{l=1,\dots,L}$ are *automatically* computed in order to guarantee continuity of the global map. In fact, once steps (A)-(B)-(C) are performed for both the coronary artery and the graft, the curve-based description of each branch is employed to compute the *known* displacement $\boldsymbol{d}_l(\boldsymbol{\eta},\boldsymbol{\eta}') = \boldsymbol{C}(\boldsymbol{p}_l;\boldsymbol{\eta},\boldsymbol{\eta}',\boldsymbol{\omega}) - \boldsymbol{p}_l$,

$l = 1, \dots, L$ of each control point on the interface between branches and anastomosis (e.g. control points denoted by green and blue markers in 5a).

Our experience suggests that at least nine additional control points should also be added in the anastomosis region (see Figures 5a (red markers) and 5b) to prevent undesired variations of the radius in the parametrized graft, especially when performing large rotations, resulting in $L = L_{\text{int}} + 9$. Also in this case their position in the deformed domain can be *automatically* computed, once step (B) has been performed for each branch. For instance, the deformed position of the control point A in Figure 5b is computed as the intersection between the straight lines AHG (lying on the plane $(\boldsymbol{t}_c, \boldsymbol{t}_g)$, parallel to $\boldsymbol{t}_c$ at a distance r_c from O, being r_c the local radius of the native coronary artery) and ABC (lying on the plane $(\boldsymbol{t}_c, \boldsymbol{t}_g)$, parallel to $\boldsymbol{t}_g(\boldsymbol{\eta}')$ at a distance r_g from O, being r_g the local radius of the graft).

Although being applied in this work for the deformation of coronary artery bypass grafts (see in particular Figure 2), the centerlines-based parametrization proposed here can be considered as a general tool to perform deformations of blood vessels, by operating on few relevant parameters related to the radius of the vessel or some control points on its centerline.

4. POD–Galerkin reduced-order models

Once a suitable mapping between a reference network and a deformed configuration is achieved by means of the centerlines-based parametrization, a parametrized formulation of the fluid dynamics problem can be obtained, as summarized e.g. in [23]. In particular, we consider the following unsteady parametrized Navier-Stokes equations, under rigid walls assumption:

$$
\begin{cases}
\frac{\partial}{\partial t}\boldsymbol{u} - \nu\Delta\boldsymbol{u} + (\boldsymbol{u}\cdot\nabla)\boldsymbol{u} + \nabla p = \boldsymbol{0} & \text{in } \Omega_o(\boldsymbol{\mu}) \times (0,T), \\
\operatorname{div}\boldsymbol{u} = 0 & \text{in } \Omega(\boldsymbol{\mu}) \times (0,T), \\
\boldsymbol{u} = \theta_D(\boldsymbol{\mu})\boldsymbol{g}_D & \text{on } \Gamma_D \times (0,T), \\
\boldsymbol{u} = \boldsymbol{0}, & \text{on } \Gamma_{o,W}(\boldsymbol{\mu}) \times (0,T), \\
\nu\dfrac{\partial \boldsymbol{u}}{\partial \boldsymbol{n}} - p\boldsymbol{n} = \boldsymbol{0}, & \text{on } \Gamma_N \times (0,T), \\
\boldsymbol{u}_{t=0} = \boldsymbol{g}_0(\boldsymbol{\mu}), & \text{in } \Omega_o(\boldsymbol{\mu}).
\end{cases}
$$

The parameters are denoted by $\boldsymbol{\mu} \in \mathcal{D} \subset \mathbb{R}^P$, including both physical quantities (e.g. multiplicative factors $\theta_D(\boldsymbol{\mu})$ on the inlet Dirichlet data $\boldsymbol{g}_D(t)$), and geometrical parameters, denoted by $\boldsymbol{\alpha}, \boldsymbol{\delta\theta}$ so fare, that provide the deformation of the patient-specific reference domain Ω to the parametrized domain $\Omega_o(\boldsymbol{\mu})$. In the same way, also its lateral boundary $\Gamma_{o,W}(\boldsymbol{\mu})$ is mapped from the reference configuration to the deformed one; without loss of generality, Γ_D (inlet sections)

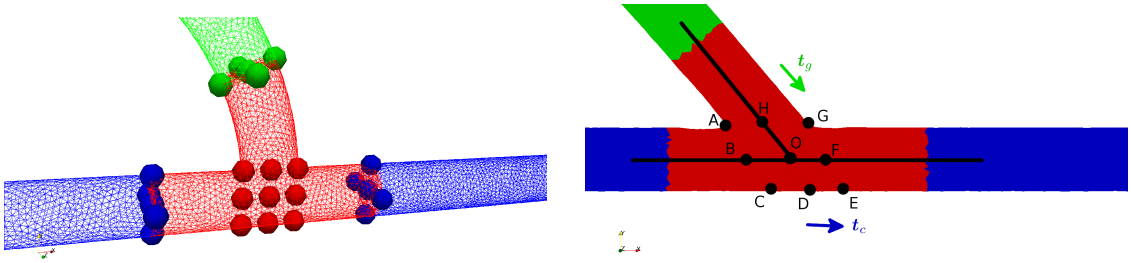

(A) Reference domain and corresponding domain decomposition (blue and green: monodimensional parametrization (3); red: three-dimensional representation (8)). Relevant choices for control points of (8).

(B) Relevant choices for a subset of the control points of (8).

Figure 5. Reference domain and relevant control point choices.

and Γ_N (outlet boundaries) are assumed to be fixed. Finally, the initial condition $\boldsymbol{g}_0$ is assumed to be the solution of a steady-state problem for the same parameters.

Since the number of parameters is relatively small thanks to the compact representation of the proposed parametrization (stenosis factors and grafting angles) a Proper Orthogonal Decomposition (POD)–Galerkin reduced-order model (ROM) can be efficiently queried to provide fast evaluation of the flow patterns. In this section we provide a summary of POD–Galerkin ROMs that we have applied to solve unsteady parametrized Navier-Stokes equations.

Since the solution of a new high-fidelity (e.g. finite elements) problem for *each* new value of the parameters (e.g. in a sensitivity analysis) is too expensive to be computed in a fast way, we rely on ROMs to obtain a faster, yet accurate, approximation. Computational savings are possible thanks to *(i)* a parametrized formulation of the problem of interest, which has motivated the development of the centerlines-based parametrization, and *(ii)* an offline-online computational splitting. During the offline stage, few high-fidelity approximations of the computational fluid dynamics problem are solved, for different parameters values. At the end of this stage, a POD is performed to build a reduced basis for the problem at hand. During the online stage, for each new value of the parameters, the reduced-order solution is obtained through a Galerkin projection over the space spanned by these basis functions, thus entailing the solution of a much smaller system. Recent contributions on these topics can be found in [9].

4.1. **Algebraic formulation of the full-order approximation.** In this section the formulation of a high-fidelity approximation of the parametrized problem at hand is recalled. This is indeed a fundamental ingredient of any ROM technique. For the sake of brevity, only the algebraic formulation of the problem will be provided; see e.g. [26, Chapter 4 and Section 5.3] for further details on the underlying continuous formulation and several test cases on simplified geometries, and [37, 38, 39] for other approaches.

Let us denote by $\boldsymbol{V}_h$ and Q_h two finite-dimensional spaces for velocity and pressure, of dimension $N_{\mathbf{u}}^h$ and N_p^h, respectively, based on a finite element (FE) discretization of the patient-specific geometry of mesh size h. Also, denote by $\{\boldsymbol{\varphi}_i^h\}_{i=1,\dots,N_{\mathbf{u}}^h}$ and $\{\zeta_k^h\}_{k=1,\dots,N_p^h}$ two bases of the FE velocity and pressure spaces, respectively. The nonlinear system of ODEs resulting from a FE discretization is: given $\boldsymbol{\mu} \in \mathcal{D}$, find $(\underline{\mathbf{u}}(t), \underline{\mathbf{p}}(t))$, being $\underline{\mathbf{u}} = (u_h^{(1)}, \dots, u_h^{(N_{\mathbf{u}}^h)})^T \in \mathbb{R}^{N_{\mathbf{u}}^h}$, $\underline{\mathbf{p}} = (p_h^{(1)}, \dots, p_h^{(N_p^h)})^T \in \mathbb{R}^{N_p^h}$ the vector of unknown FE coefficients, such that

$$\begin{bmatrix} M(\boldsymbol{\mu}) & 0 \\ 0 & 0 \end{bmatrix} \begin{bmatrix} \dot{\underline{\mathbf{u}}}(t;\boldsymbol{\mu}) \\ \dot{\underline{\mathbf{p}}}(t;\boldsymbol{\mu}) \end{bmatrix} + \begin{bmatrix} \nu A(\boldsymbol{\mu}) + C(\underline{\mathbf{u}}(t;\boldsymbol{\mu});\boldsymbol{\mu}) & B^T(\boldsymbol{\mu}) \\ B(\boldsymbol{\mu}) & 0 \end{bmatrix} \begin{bmatrix} \underline{\mathbf{u}}(t;\boldsymbol{\mu}) \\ \underline{\mathbf{p}}(t;\boldsymbol{\mu}) \end{bmatrix} = \begin{bmatrix} \underline{\mathbf{f}}(t) \\ \underline{\mathbf{0}} \end{bmatrix}, \quad (4)$$

where $\underline{\mathbf{u}}(0)$ is chosen equal to the FE interpolant of the initial condition, and the right-hand side term $\underline{\mathbf{f}}(t)$ encodes non-homogeneous Dirichlet boundary conditions through a lifting. The parametrized tensors appearing in (4) are defined as follows: for $1 \le i, j \le N_{\mathbf{u}}^h$ and $1 \le k \le N_p^h$:

$$\begin{gathered} A_{ij}(\boldsymbol{\mu}) = \int_\Omega \nabla\boldsymbol{\varphi}_j^h \, \boldsymbol{\kappa}(\boldsymbol{x},t;\boldsymbol{\mu}) : \nabla\boldsymbol{\varphi}_i^h \, d\boldsymbol{x}, \quad B_{ki}(\boldsymbol{\mu}) = -\int_\Omega \zeta_k^h \, \mathrm{tr}(\boldsymbol{\chi}(\boldsymbol{x};\boldsymbol{\mu}) \, \nabla\boldsymbol{\varphi}_i^h) \, d\boldsymbol{x} \\ C_{ij}(\underline{\mathbf{u}}(\boldsymbol{\mu});t;\boldsymbol{\mu}) = \sum_{m=1}^{N_{\mathbf{u}}^h} u_h^{(m)}(t;\boldsymbol{\mu}) \int_\Omega (\nabla\boldsymbol{\varphi}_j^h \, \boldsymbol{\chi}(\boldsymbol{x};\boldsymbol{\mu}))\boldsymbol{\varphi}_m^h \cdot \boldsymbol{\varphi}_i^h \, d\boldsymbol{x}; \\ M_{ij}(\boldsymbol{\mu}) = \int_\Omega \pi(\boldsymbol{x};\boldsymbol{\mu}) \, \boldsymbol{\varphi}_j^h \cdot \boldsymbol{\varphi}_i^h \, d\boldsymbol{x}, \end{gathered} \quad (5)$$

here we denote by

$$\begin{aligned} \boldsymbol{\kappa}(\boldsymbol{x};\boldsymbol{\mu}) &= (J_{\boldsymbol{T}}(\boldsymbol{x};\boldsymbol{\mu}))^{-1} (J_{\boldsymbol{T}}(\boldsymbol{x};\boldsymbol{\mu}))^{-T} |J_{\boldsymbol{T}}(\boldsymbol{x};\boldsymbol{\mu})| \\ \boldsymbol{\chi}(\boldsymbol{x};\boldsymbol{\mu}) &= (J_{\boldsymbol{T}}(\boldsymbol{x};\boldsymbol{\mu}))^{-1} |J_{\boldsymbol{T}}(\boldsymbol{x};\boldsymbol{\mu})|, \quad \pi(\boldsymbol{x};\boldsymbol{\mu}) = |J_{\boldsymbol{T}}(\boldsymbol{x};\boldsymbol{\mu})|, \end{aligned}$$

the tensors $\boldsymbol{\kappa}, \boldsymbol{\chi}$, and the scalar π encoding both physical and geometrical parametrization. We recall that $J_{\boldsymbol{T}} \in \mathbb{R}^{3\times3}$ is the Jacobian matrix of the map $\boldsymbol{T}(\cdot;\ \boldsymbol{\alpha},\ \boldsymbol{\delta\theta})$ defined by (2), and $|J_{\boldsymbol{T}}|$ denotes its determinant.

The resulting nonlinear system after a time discretization with the Implicit Euler scheme is: given $\boldsymbol{\mu} \in \mathcal{D}$ and $(\underline{\mathbf{u}}(t^n), \underline{\mathbf{p}}(t^n))$, find $(\underline{\mathbf{u}}(t^{n+1}), \underline{\mathbf{p}}(t^{n+1}))$ such that

$$\begin{bmatrix} \frac{M(\boldsymbol{\mu})}{\Delta t} + \nu A(\boldsymbol{\mu}) + C(\underline{\mathbf{u}}(t^{n+1};\boldsymbol{\mu});\boldsymbol{\mu}) & B^T(\boldsymbol{\mu}) \\ B(t^{n+1};\boldsymbol{\mu}) & 0 \end{bmatrix} \begin{bmatrix} \underline{\mathbf{u}}(t^{n+1};\boldsymbol{\mu}) \\ \underline{\mathbf{p}}(t^{n+1};\boldsymbol{\mu}) \end{bmatrix} = \begin{bmatrix} \frac{M(\boldsymbol{\mu})}{\Delta t}\underline{\mathbf{u}}(t^n;\boldsymbol{\mu}) + \underline{\mathbf{f}}(t^{n+1}) \\ \underline{\mathbf{0}} \end{bmatrix};$$

at each time-step $n = 0, \dots, T/\Delta t - 1$, the nonlinear system is solved by means of a Newton method (see e.g. [23, 40] for more details).

4.2. **Reduced basis construction through Proper Orthogonal Decomposition.** Let us denote by $\Xi_{\text{train}} = \{\boldsymbol{\mu}^1, \dots, \boldsymbol{\mu}^{N_{\text{train}}}\} \subset \mathcal{D}$ a training sample of N_{train} points chosen randomly over the parameter space $\mathcal{D}$. For each point $(i = 1, \dots, N_{\text{train}})$ in the training sample a FE solve of unsteady Navier Stokes equations is performed. Moreover, following the approach analyzed in [23, 41, 42], to enhance the stability of the resulting reduced-order approximation in order to obtain a more accurate pressure recovery, at each time step the following elliptic problem

$$X_{\mathbf{u}} \underline{\mathbf{s}}(\underline{\mathbf{p}}(t^n;\boldsymbol{\mu}^i)) = B^T(\boldsymbol{\mu}^i)\underline{\mathbf{p}}(t^n;\boldsymbol{\mu}^i), \quad i = 1, \dots, N_{\text{train}} \tag{6}$$

is solved to obtain the so-called supremizer solution $\underline{\mathbf{s}}(\underline{\mathbf{p}}(t^n;\boldsymbol{\mu}^i))$, where $X_{\mathbf{u}} \in \mathbb{R}^{N^h_{\mathbf{u}} \times N^h_{\mathbf{u}}}$ is the FE matrix of the inner product on $\boldsymbol{V}_h$.

The temporal evolution of the full-order solutions is stored in the following *snapshot matrices on the temporal trajectory*:

$$\begin{aligned} S^i_{\mathbf{u}} &= [\widehat{\underline{\mathbf{u}}}(t^1;\boldsymbol{\mu}^i) \mid \dots \mid \widehat{\underline{\mathbf{u}}}(t^{N^t};\boldsymbol{\mu}^i)] \in \mathbb{R}^{N^h_{\mathbf{u}} \times N^t}, \quad \forall i = 1, \dots, N_{\text{train}}, \\ S^i_p &= [\underline{\mathbf{p}}(t^1;\boldsymbol{\mu}^i) \mid \dots \mid \underline{\mathbf{p}}(t^{N^t};\boldsymbol{\mu}^i)] \in \mathbb{R}^{N^h_p \times N^t}, \quad \forall i = 1, \dots, N_{\text{train}}, \\ S^i_{\mathbf{s}} &= [\underline{\mathbf{s}}(\underline{\mathbf{p}}(t^1;\boldsymbol{\mu}^i)) \mid \dots \mid \underline{\mathbf{s}}(\underline{\mathbf{p}}(t^{N^t};\boldsymbol{\mu}^i))] \in \mathbb{R}^{N^h_{\mathbf{u}} \times N^t}, \quad \forall i = 1, \dots, N_{\text{train}}. \end{aligned}$$

The notation $\widehat{\underline{\mathbf{u}}}(t^n;\boldsymbol{\mu}^i)$ refers to the difference between the full-order solution $\underline{\mathbf{u}}(t^n;\boldsymbol{\mu}^i)$ and lifting functions at $t = t^n$ and $\boldsymbol{\mu} = \boldsymbol{\mu}^i$ to account for inhomogeneous boundary conditions.

The following *snapshot matrices on the temporal trajectory and parameter space* are assembled,

$$\begin{aligned} S_{\mathbf{u}} &= [S^1_{\mathbf{u}} | \dots | S^{N_{\text{train}}}_{\mathbf{u}}] \in \mathbb{R}^{N^h_{\mathbf{u}} \times (T/\Delta t \cdot N_{\text{train}})}, \\ S_p &= [S^1_p | \dots | S^{N_{\text{train}}}_p] \in \mathbb{R}^{N^h_p \times (T/\Delta t \cdot N_{\text{train}})}, \\ S_{\mathbf{s}} &= [S^1_{\mathbf{s}} | \dots | S^{N_{\text{train}}}_{\mathbf{s}}] \in \mathbb{R}^{N^h_{\mathbf{u}} \times (T/\Delta t \cdot N_{\text{train}})}. \end{aligned}$$

and a POD is performed for each matrix. The first $N_{\mathbf{u}}, N_p, N_{\mathbf{s}}$ (respectively) left singular vectors are considered as basis functions $\{\boldsymbol{\varphi}_n\}_{n=1}^{N_{\mathbf{u}}}, \{\zeta_n\}_{n=1}^{N_p}, \{\boldsymbol{\eta}_n\}_{n=1}^{N_{\mathbf{s}}}$. The reduced spaces for velocity $\boldsymbol{V}_N$ and pressure Q_N, of cardinality $N_{\mathbf{u},\mathbf{s}} = N_{\mathbf{u}} + N_{\mathbf{s}}$ and N_p are then obtained as

$$\boldsymbol{V}_N = \text{span}(\{\boldsymbol{\varphi}_n\}_{n=1}^{N_{\mathbf{u}}}, \{\boldsymbol{\eta}_n\}_{n=1}^{N_{\mathbf{s}}}) \quad \text{and} \quad Q_N = \text{span}(\{\zeta_n\}_{n=1}^{N_p}).$$

In view of the Galerkin projection, the corresponding basis functions matrices

$$Z_{\mathbf{u},\mathbf{s}} = [\boldsymbol{\varphi}_1 | \dots | \boldsymbol{\varphi}_{N_{\mathbf{u}}} | \boldsymbol{\eta}_1 | \dots | \boldsymbol{\eta}_{N_{\mathbf{s}}}] \in \mathbb{R}^{N^h_{\mathbf{u}} \times N_{\mathbf{u}}} \quad \text{and} \quad Z_p = [\zeta_1 | \dots | \zeta_{N_p}] \in \mathbb{R}^{N^h_p \times N_p}$$

are also introduced.

4.3. **Algebraic formulation of the POD-Galerkin ROM.** A reduced-order approximation of both velocity and pressure fields is obtained by means of a Galerkin projection on the reduced spaces $\boldsymbol{V}_N$ and Q_N. In particular, we seek an approximation of the form

$$\underline{\mathbf{u}}(t;\boldsymbol{\mu}) \approx Z_{\mathbf{u},\mathbf{s}}\underline{\mathbf{u}}_N(t;\boldsymbol{\mu}), \qquad \underline{\mathbf{p}}(t;\boldsymbol{\mu}) \approx Z_p\underline{\mathbf{p}}_N(t;\boldsymbol{\mu}),$$

In the online stage, the resulting reduced-order approximation of the parametrized unsteady Navier-Stokes problems reads: for any $\boldsymbol{\mu} \in \mathcal{D}$, given $\underline{\mathbf{u}}_N(t^n;\boldsymbol{\mu})$, solve

$$\begin{bmatrix} \frac{M_N(\boldsymbol{\mu})}{\Delta t} + \nu A(\boldsymbol{\mu}) + C_N(\underline{\mathbf{u}}_N(t^{n+1};\boldsymbol{\mu});\boldsymbol{\mu}) & B^T_N(\boldsymbol{\mu}) \\ B_N(\boldsymbol{\mu}) & 0 \end{bmatrix} \begin{bmatrix} \underline{\mathbf{u}}_N(t^{n+1};\boldsymbol{\mu}) \\ \underline{\mathbf{p}}_N(t^{n+1};\boldsymbol{\mu}) \end{bmatrix} = \begin{bmatrix} \frac{M_N(\boldsymbol{\mu})}{\Delta t}\underline{\mathbf{u}}_N(t^n;\boldsymbol{\mu}) + \underline{\mathbf{f}}_N(t^{n+1}) \\ \underline{\mathbf{0}} \end{bmatrix},$$

for any $n = 0, \dots, T/\Delta t - 1$, where, similarly to [23],

$$A_N(\boldsymbol{\mu}) = Z_{\mathbf{u},\mathbf{s}}^T \; A(\boldsymbol{\mu}) \; Z_{\mathbf{u},\mathbf{s}}, \qquad B_N(\boldsymbol{\mu}) = Z_p^T \; B(\boldsymbol{\mu}) \; Z_{\mathbf{u},\mathbf{s}}, \qquad C_N(\,\cdot\,;\boldsymbol{\mu}) = Z_{\mathbf{u},\mathbf{s}}^T C(\,\cdot\,;\boldsymbol{\mu}) Z_{\mathbf{u},\mathbf{s}}.$$

As in the FE approximation, the initial condition $\underline{\mathbf{u}}_N(0;\boldsymbol{\mu})$ is the solution of a reduced-order steady-state Navier-Stokes problem.

In order to guarantee an offline-online splitting, and thus high computational savings, an affine parametric dependence assumption on (5) is made, e.g.

$$A(\boldsymbol{\mu}) = \sum_{q=1}^{Q_A} \Theta_q^A(\boldsymbol{\mu}) A^q, \quad C(\underline{\mathbf{w}};\boldsymbol{\mu}) = \sum_{q=1}^{Q_C} \Theta_q^C(\boldsymbol{\mu}) C^q(\underline{\mathbf{w}})$$

for some parameter dependent factors $\Theta_q^*(\boldsymbol{\mu})$, and in a similar way for the other terms. Thanks to this assumption, only the matrices and vectors

$$A_N^q = Z_{\mathbf{u},\mathbf{s}}^T \; A^q \; Z_{\mathbf{u},\mathbf{s}}, \qquad B_N^q = Z_p^T \; B^q \; Z_{\mathbf{u},\mathbf{s}}, \qquad C_N^q(\,\cdot\,) = Z_{\mathbf{u},\mathbf{s}}^T C^q(\,\cdot\,) Z_{\mathbf{u},\mathbf{s}},$$

need to be stored. Due to the non-affinity of the centerlines-based parametrization, the Empirical Interpolation Method [43] is applied to the parametrized tensors $\boldsymbol{\kappa}, \boldsymbol{\chi}$, and the scalar π in order to recover the affine parametric dependence. The number of terms Q_A, $Q_B = Q_C$ and Q_M in the affine expansion, and its relation to online computational times, will be discussed in the next section. As for the full-order approximation, at each time the online nonlinear system is solved by means of Newton iterations.

5. Numerical results

In this section we exploit the reduced-order computational framework introduced so far to study the haemodynamics with respect to the following parameters:

- *inlet flow rates*: different rest or stress conditions are taken into account by means of a variation of inlet flow rates. In fact, an increased blood flow to the heart is required under stress conditions, and blood flow in coronary arteries is increased in response to this need. Physical parameters are related to the variation of inlet flow rates of left coronary artery, right coronary artery (if studied) and bypass grafts. These parameters will be denoted in the following by f^b, for $b =$ LITA, LCA, RCA and are multiplicative factors on inlet flow rates adapted from literature (LCA and RCA [44], LITA [45]);
- *stenosis severities* $\boldsymbol{\alpha}$: graft patency rates are related to proximal stenosis severity [1]. The centerlines-based geometrical parametrization of a single vessel, proposed in Section 3.1, allows an easy and intuitive application to the variation of the severity of the stenosis by performing local variations on the radius of the vessel. Analyzing the sensitivity of the haemodynamics with respect to the severity of a stenosis is interesting from a clinical standpoint. In fact, current medical experience suggests that surgery should be performed only for critical occlusions;
- *grafting angles* $\boldsymbol{\delta\theta}$ *and local anastomosis configuration*: tissue remodeling and intimal hyperplasia are highly sensitive to the graft configuration near the anastomosis [36, 5]. To investigate possible different anastomoses, the variation of the angle between the graft and the native vessel is studied as proposed in Section 3.2.

Numerical results in this section will be presented for pressure drop across stenoses[4] and wall shear stress near anastomoses. Indeed, pressure drop across stenoses is a possible indicator, yet invasive in the clinical practice, of the presence and severity of a stenosis, and wall shear stress has been related to the process of reocclusion of grafts [6].

5.1. **Computational performances of the proposed reduced-order framework.** Details of the reduced-order model are summarized in Table 1. The number of considered physical

[4]Since the standard deviation σ, introduced in Section 3.1, is a measure of the "extension" of the stenosis, the pressure drop is computed as the difference between the average pressure of sections at distance -3σ and $+3\sigma$ from the center μ of the stenosis.

Patient	**1*f***	**1*s***	**4*f***	**7*s***	**13*s***	**15*a***
Num. physical parameters	6	6	4	4	6	0
LCA inlet flow rate parameters	1	1	1	1	1	no
RCA inlet flow rate parameters	1	1	no	no	1	no
LITA inlet flow rate parameters	1	1	1	1	1	no
Num. geometrical parameters	0	3	0	3	4	2
LCA parametrized stenosis	no	no	no	1	no	no
LAD/Diag parametrized stenosis	no	1	no	1	2	1
LCX/OM parametrized stenosis	no	1	no	1	1	no
RCA parametrized stenosis	no	1	no	no	1	no
Parametrized anastomosis	no	no	no	no	no	1
FE velocity order	2					
FE pressure order	1					
Total number of FE dofs	1 325 530	1 325 530	1 325 044	970 618	1 426 060	1 219 918
Temporal step	0.01					
Num. time steps/cardiac cycle	80					
FE CPU time/cardiac cycle	$11 \sim 13$ h	$11 \sim 13$ h	$11 \sim 13$ h	$9 \sim 12$ h	$9 \sim 11$ h	$11 \sim 13$ h
ROM CPU time/cardiac cycle	$2 \sim 3$ min	$5 \sim 15$ min	$2 \sim 3$ min	$5 \sim 15$ min	$5 \sim 15$ min	$25 \sim 35$ min
$N_{\mathbf{train}}$	50					
$N_{\mathbf{max}}$	50					
Q_M, Q_A, $Q_B = Q_C$	1, 1, 1	14, 36, 37	1, 1, 1	19, 42, 40	19, 48, 33	37, 133, 53

TABLE 1. Details of the reduced-order model for six different representative cases. Patient suffix f stands for flow rate parametrization; s for stenosis and flow rate parametrization; a for anastomosis parametrization.

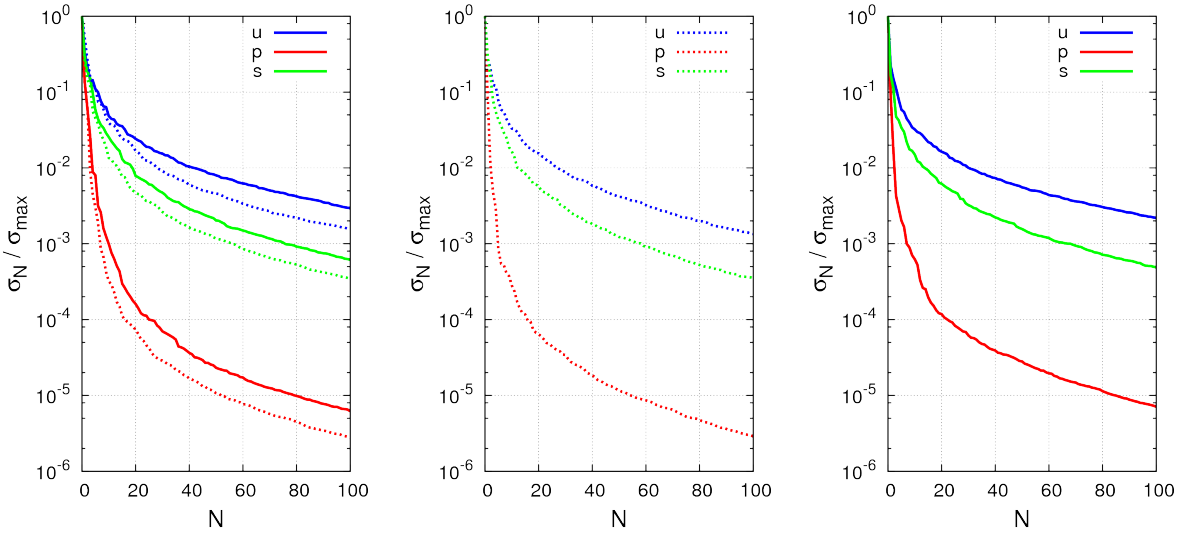

(A) **Patient 1*f* and 1*s*.** (B) **Patient 4*f*.** (C) **Patient 7*s*.**

FIGURE 6. Results of the offline stage for four cases of Table 1: POD singular values for velocity, supremizers, pressure (dotted lines: flow rate parametrization only, solid lines: flow rate and stenosis parametrization).

and geometrical parameters is reported for each patient. The location of the stenoses is also summarized in the table, and has been obtained from available clinical data.

A Taylor-Hood $\mathbb{P}_2 - \mathbb{P}_1$ FE discretization is employed for the space discretization; an Implicit Euler method is considered for the time discretization. N_{train} unsteady FE problems are solved

for randomly chosen parameters values; each FE solution accounts for 80 time steps per cardiac cycle, for 2 cardiac cycles. A POD–Galerkin ROM is obtained, considering the first $N_{\max}$ modes.

The offline stage is performed in parallel, taking advantage of 32 processors on modern HPC clusters. In case of geometrical parametrization, the offline stage of the POD–Galerkin method contains also the offline stage of the EIM preprocessing to obtain the affine expansion of the Navier-Stokes operators. The resulting number of affine expansion components Q_M, Q_A and $Q_B = Q_C$ are shown in Table 1. EIM offline stage requires usually about $5 \sim 7$ hours to reach a tolerance of 10^{-3}, for an EIM training set of 500 points. This a preprocessing stage, which is done only once. The truth solution for each sample point (and for each cardiac cycle) requires approximately 10 hours (to be multiplied by the number of processors to obtain the actual CPU time). The online stage, instead, is performed on a single processor. Each online online ROM solution requires only few minutes, thanks to the considerable reduction in the number of degrees of freedom ($N_{\mathbf{u}} = N_{\mathbf{s}} = N_p = N_{\max}$) and efficient offline-online procedure, with computational savings in terms of user time up to 99%. Online CPU times are higher in the case of geometrical parametrization because of larger affine expansions and higher number of nonlinear iterations, but computational savings are nevertheless remarkable also in this case (more than 95%).

Figure 6 shows a plot of the POD singular values for velocity, supremizers, pressure variables for a single patient. The pattern is also similar for the other studied patients; in all cases velocity (and supremizers) feature a considerably slower decay than pressure. A comparison, on the same patient, between the case of flow rate parametrization only (dotted lines) and flow rate parametrization and stenosis variation (solid lines) is also shown. Slower decay is the result of additional geometrical parameters.

5.2. **Comparison between full-order and reduced-order simulations.** The comparison between full-order and reduced-order simulations is provided in Figure 7 for Patient 4*f*, considering a flow rate parametrization (multiplicative factors f^{LCA} and f^{LITA} on a prescribed flow rate profile). A summary of the surgery is provided in Figure 7(a): a mammary artery bypass graft is employed in a sequential fashion to revascularize the left coronary tree, and in particular a diagonal branch and the left anterior descending one. The full-order solution is provided in Figure 7(b). Figures 7(c)-(f) show reduced-order solutions for different number of basis functions. This analysis shows that the full-order solution is accurately described increasing the number of online degrees of freedom $N = N_{\mathbf{u}} = N_{\mathbf{s}} = N_p$. This analysis also shows that if too few basis functions are considered, say $N = 1$, then the reduced-order solution does not agree with the full-order one. The pattern of the WSS in the anastomosis is not represented accurately, and peak values in the anastomosis are considerably underestimated, being less than 50% of the full-order peak WSS. In contrast, increasing the value of N good qualitative agreement of the WSS patterns can be obtained at $N = 5$. The pattern in the anastomosis now more closely resembles the one of the truth solve, although the magnitude of the WSS is overestimated (relative error of approximately 30%). Better quantitative agreement are obtained increasing further $N = 20$ (error of approximately 5%), and, in particular, a good approximation of the full-order solution is obtained in this case at $N = 30$ (error below 1%), which is still considerably lower than the number of full-order degrees of freedom, of the order of 10^6.

5.3. **Comparison of flow patterns in parametrized patient-specific configurations.** In this section we further elaborate on the flow patterns obtained employing the reduced-order framework on two parametrized patient-specific configurations.

Different flow patterns are found in Patient 1*f* depending on the parametrized flow rate. Although this patient features an highly complex surgical procedure (quadruple bypass), for the sake of exposition we will focus on a single anastomosis in Figure 8(a), between a mammary artery bypass graft (LITA) and the left anterior descending (LAD). Figure 8(b) and (c) show a comparison of time-averaged wall shear stress near anastomosis for different inflow boundary conditions, corresponding to standard ($f^{LITA} = 1$) and increased graft flow rates ($f^{LITA} = 1.33$). The proposed reduced-order framework captures different physical behavior: a region of

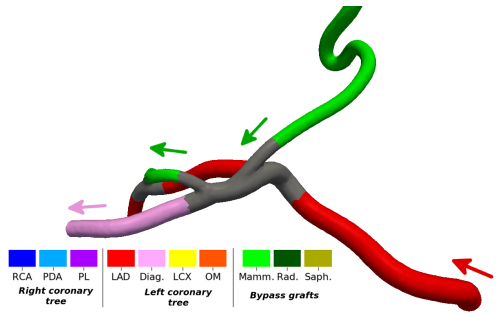

(A) Coronary arteries and bypass grafts near the studied anastomoses. Colored arrows denote blood flow direction.

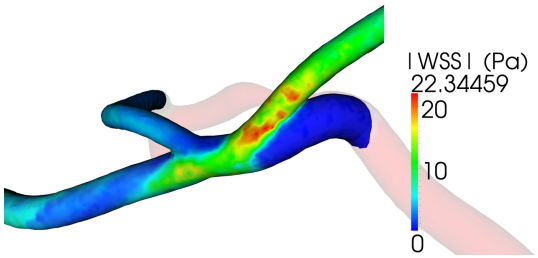

(B) Full-order solution.

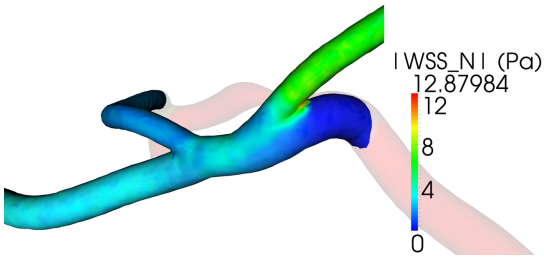

(C) Reduced-order solution, $N = 1$.

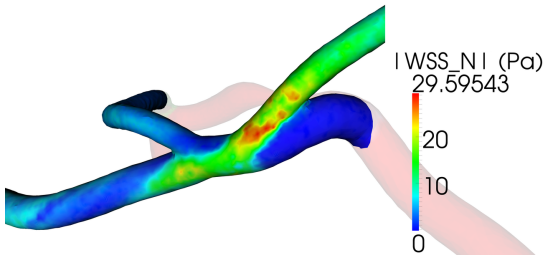

(D) Reduced-order solution, $N = 5$.

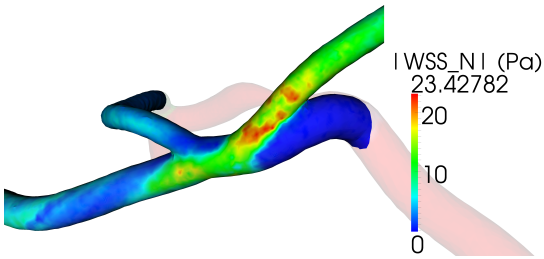

(E) Reduced-order solution, $N = 20$.

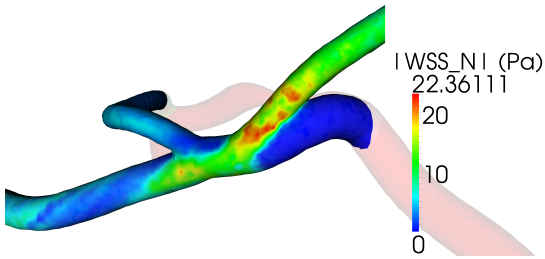

(F) Reduced-order solution, $N = 30$.

FIGURE 7. **Patient 4*f* - LITA-Diag anastomosis**. Comparison of wall shear stress: full-order solution and reduced-order solutions, for increasing N. The multiplicative factor f^{LCA} and f^{LITA} are chosen equal to 1.

locally high wall shear stress is found on the graft near the anastomosis, and in the arterial bed; higher WSS on the graft and a larger region of WSS on the arterial bed are due to increased graft flow rate.

A similar analysis can be performed on Patient 13*s*, varying the entity of stenosis and flow rates. The surgery features a quadruple bypass, revascularizing both the left and right coronary artery by means of a Y-graft (a bifurcation between two grafts, created during the surgery) between the LITA and a saphenous vein graft (SVG). The anastomosis analyzed in Figure 9(a) is a latero-lateral cross anastomosis between SVG and the left circumflex branch (LCX) in the left coronary tree. A region of high WSS is located on the arterial bed distal to the cross anastomosis. Increased LCX flow rates, both as a consequence of increased native LCA flow rates or decreased stenosis, have a significant impact on the local pattern of the WSS in this region. This is particularly evident especially in figures (d) and (e), for increased flow rates in the graft.

5.4. **Evaluation of heamodynamic indices on stenosis variation in the pre-surgical case.** The fast evaluation of the proposed reduced-order framework allows to provide, in a cheap

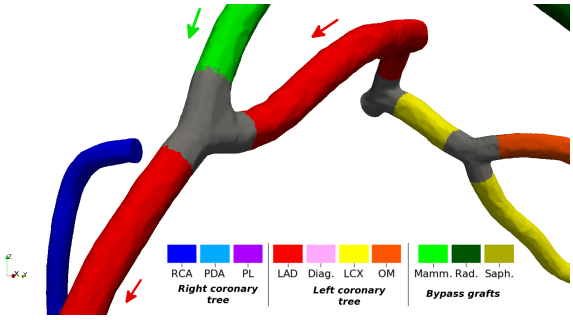

(A) Coronary arteries and bypass grafts near the studied anastomosis. Colored arrows denote blood flow direction.

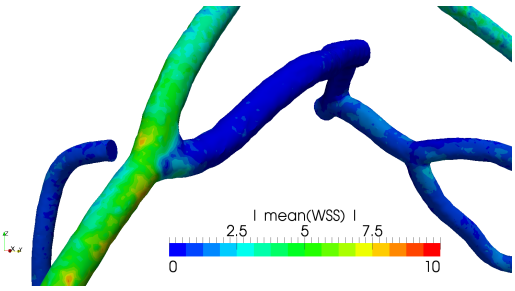

(B) Standard graft flow rate.

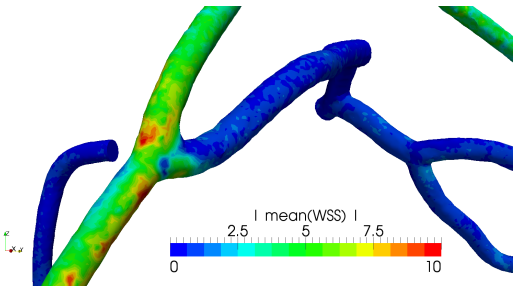

(C) Increased graft flow rate.

FIGURE 8. **Patient 1*f* - LITA to LAD anastomosis**. Comparison of time-averaged wall shear stress [Pa] for different inflow boundary conditions.

and very fast way, insights on how relevant haemodynamics quantities, such as wall shear stresses (Figure 10 for Patient 7*s*) and pressure drops (Figure 11 for Patient 1*s*) at stenosis, depend on stenosis factors and flow rates. The maximum value of wall shear stress at two stenoses (LCA, LCX) is computed. Resulting patterns are reported in Figure 10, and show a monotonically increasing value of WSS, both with respect to inlet flow rates and stenosis severity. WSS is higher in the LCA stenosis than in the LCX one; this is motivated by the fact that the blood flow in the LCA is split between two branches (LAD and LCX). Figure 11 shows the computation of the the pressure drop at the stenosis. For each one of the considered stenosis an increasing pressure drop is observed both with Reynolds number and stenosis severity. The availability of such kind of plots in the pre-surgical phase is of utmost interest in the clinical practice. In fact, clinical exams to detect the presence of a stenosis, such as cardiac catheterization, are based on experimental measures of pressure drops. Once pressure drop across stenosis is measured, plots in Figure 11 can then be employed to precisely quantify the severity of the stenosis, locating the isoline corresponding to the measured pressure drop. We further remark that, without the proposed computational reduction framework, the computational times to obtain similar plots would be unbearable in the clinical practice; in contrast, our framework allows to obtain considerably faster computations.

5.5. **Sensitivity analysis on anastomosis variation in the post-surgical phase.** A sensitivity analysis on the surgical procedure is presented as a final application of the proposed reduced-order parametrized formulation of haemodynamics in patient-specific CABGs. The analysis is carried out for Patient 15*a*, who has undergone a single bypass surgery on the left anterior descending artery. The anastomosis between native artery and bypass graft is parametrized as a function of the grafting angle θ, and the centerlines-based parametrization is employed to perform the required geometrical variation. Thanks to the fast evaluation of the reduced-order model it is possible to study the behavior of the WSS for several different configurations characterized by different grafting angles θ: antegrade (or flow-direction, $\theta \ll 90°$),

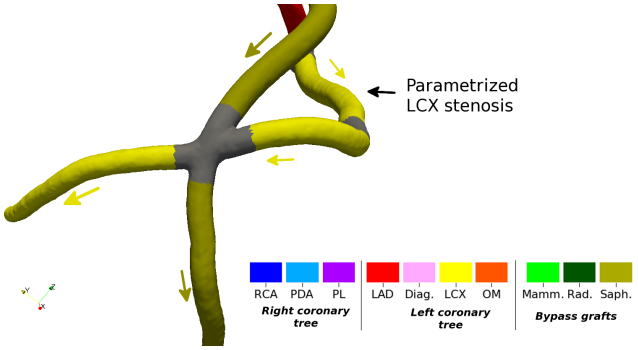

(A) Coronary arteries and bypass grafts near the studied anastomoses. Colored arrows denote blood flow direction.

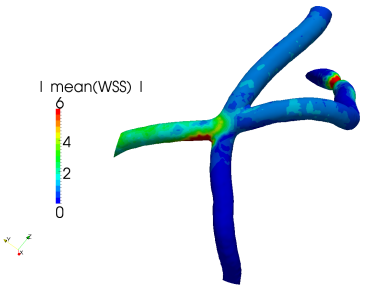

(B) Standard graft flow rate, 90% stenosis.

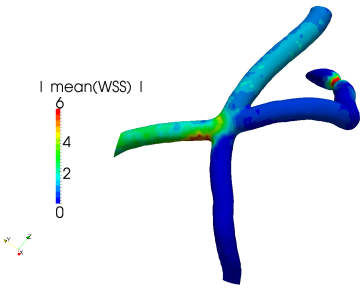

(C) Standard graft flow rate, 70% stenosis.

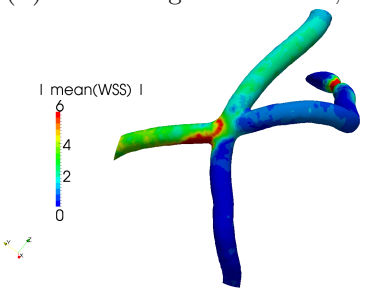

(D) Increased graft flow rate, 90% stenosis.

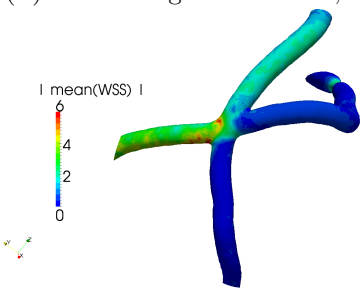

(E) Increased graft flow rate, 70% stenosis.

FIGURE 9. **Patient 13*s* - SVG-LCX anastomosis**. Comparison of time-averaged wall shear stress for different inflow boundary conditions and stenosis.

T-shaped ($\theta \approx 90°$) and retrograde-flow ($\theta \gg 90°$) anastomoses. Figure 12(a) shows the maximum WSS at the arterial bed as a function of the anastomosis angle and time. This plot shows, that WSS increases with the grafting angle at $t = 0.15$ s and $t = 0.55$ s. Figures 12(b)-(c) also show the WSS at the heel of the anastomosis. For small anastomosis angles (antegrade anastomoses) WSS at the heel and at the arterial floor are comparable in the whole time interval, except that in a neighborhood of $t = 0.4$, when WSS at the heel is smaller than WSS at the bed. This is the most favorable condition. In contrast, for larger anastomosis angles, the ratio between WSS at the heel and WSS at the arterial floor is smaller than one, except for $t = 0.4$ s. Local minima are found near T-shaped configurations: this is caused both by the increasing WSS at the arterial floor, and WSS at the heel that is decreasing for $\theta < 90°$ and increasing for $\theta > 90°$.

6. Conclusions

In this work a computational reduction framework for the study of the haemodynamics in patient-specific configurations of coronary artery bypass grafts (CABGs) has been proposed, based on the combination of a new vascular shape parametrization technique and reduced-order models for parametrized PDEs in CFD. A medical imaging pipeline for clinical data integration

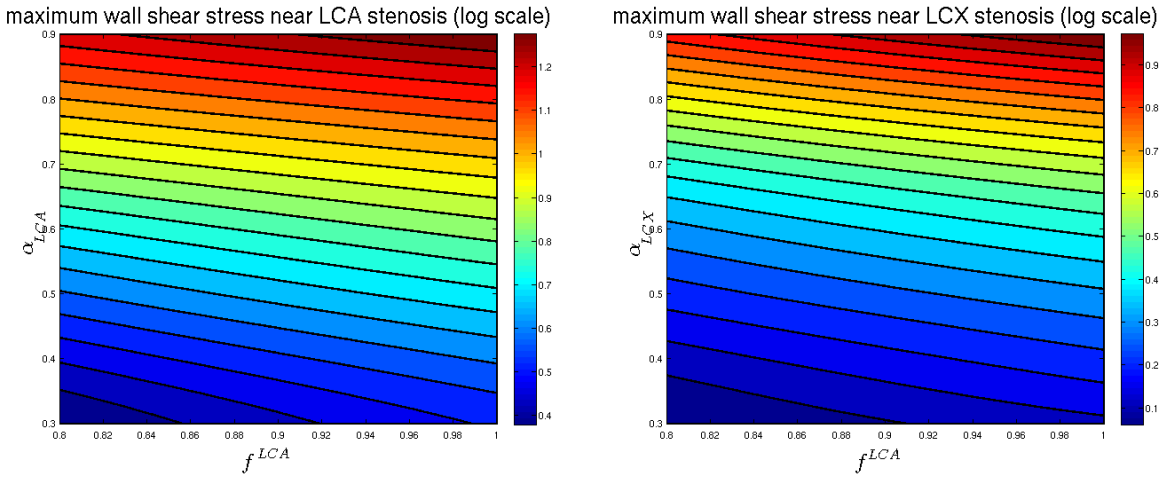

(A) LCA stenosis (B) LCX stenosis

FIGURE 10. **Patient 7*s***. Dependence of the maximum wall shear stress [Pa] near the stenosis on Reynolds number and stenosis factors.

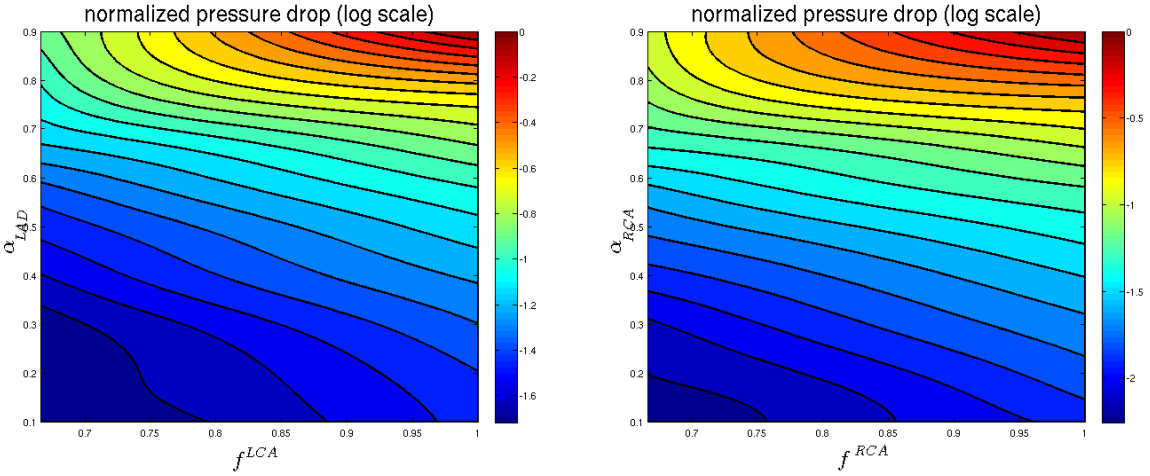

(A) LAD stenosis (B) RCA stenosis

FIGURE 11. **Patient 1*s***. Dependence of the normalized pressure drop at the stenosis on Reynolds number and stenosis factors.

and reconstruction has been introduced, assuming that coronary arteries and bypass grafts can be represented as tubular structures around vessel centerlines, in order to obtain a cylindrical representation of each branch. This assumption is the motivating idea of the new centerlines-based parametrization proposed in this work, which combines a curve-based deformation of each branch to a volume-based parametrization near anastomoses and bifurcations. The main feature of the proposed technique is the very small amount of geometrical parameters necessary to perform clinically relevant deformations on patient-specific geometries, such as stenosis and anastomosis variation. A sensitivity analysis study can then be carried out, thanks to the mapping between a patient-specific reference and a virtual deformed configuration. To avoid computationally expensive numerical simulations based e.g. on finite element approximation for *each* new configuration, a POD–Galerkin reduced-order model is employed, providing considerable computational savings and preserving very good accuracy when compared to full-order finite element simulations. The resulting reduced-order framework is then applied to several patient-specific cases, discussing computational performances with savings up to 99%

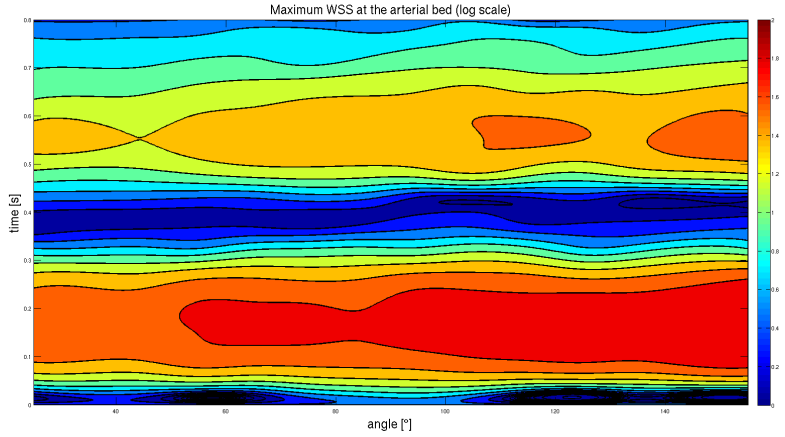

(A) Maximum wall shear stress [Pa] at the arterial bed as a function of the anastomosis angle.

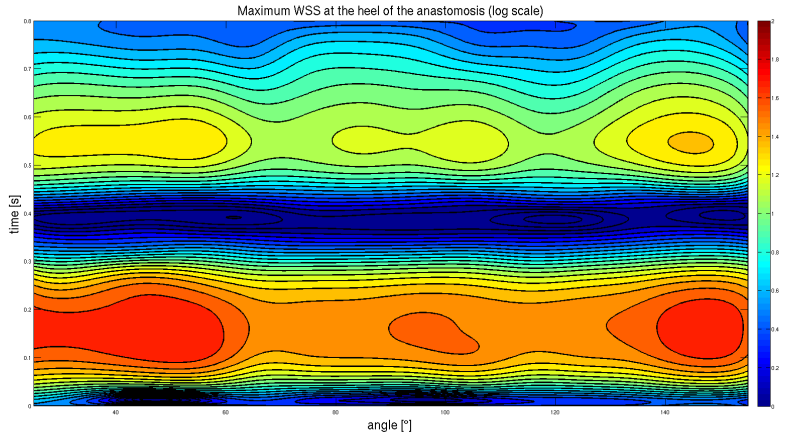

(B) Maximum wall shear stress [Pa] at the heel of the anastomosis as a function of the anastomosis angle.

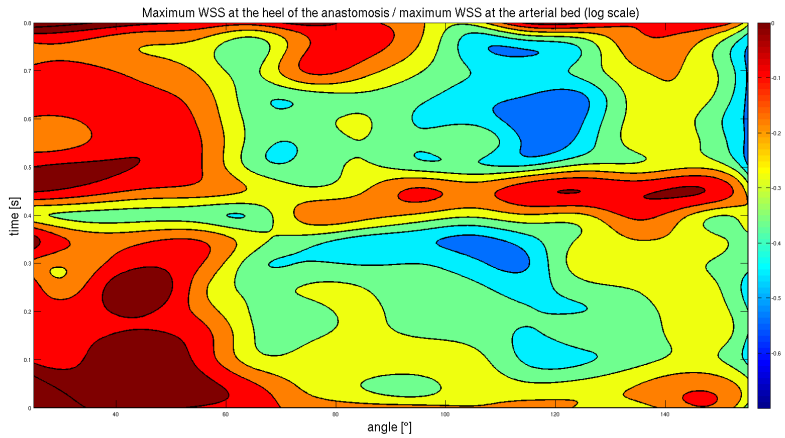

(C) Ratio between maximum wall shear stress at the heel of the anastomosis over maximum wall shear stress at the arterial bed as a function of the anastomosis angle.

FIGURE 12. **Patient 15*a* - LITA to LAD anastomosis (termino-lateral)**. Dependence of the maximum wall shear stress [Pa] on the anastomosis angle, at different locations near the anastomosis.

of CPU time. Moreover, comparison between full-order and reduced-order simulations showed that O(10 $\sim$ 100) degrees of freedom are required to obtain a reliable approximation of the haemodynamics. Visualization of flow patterns in some representative cases and applications in the clinical practice have also been provided. Similar computations would have been computationally unfeasible without the proposed reduced-order framework. The reader interested in additional clinical results obtained with the proposed reduced-order framework is referred to [46]. The reduced-order framework proposed in this work offers a powerful tool for simulations of patient-specific haemodynamics that may be applied to further problems characterized by *(i)* complex geometries, *(ii)* variation of some parameters of interest and *(iii)* need for fast evaluations, possibly favoring a more widespread usage of mathematical models in the study of complex patient-specific geometries.

Acknowledgments

We acknowledge the use CINECA supercomputing facilities within the projects "Convenzione di Ateneo" agreement between Politecnico di Milano and CINECA, and "COGESTRA" between SISSA and CINECA, and Istituto Nazionale di Fisica Nucleare, within the project SUMA. We acknowledge the use of a customized version of the library `rbOOmit` within `libMesh` [47, 48] for the numerical simulations, and of the Vascular Modelling Toolkit `vmtk` [24] and `3DSlicer` [25] for the medical imaging pipeline. Francesco Ballarin and Elena Faggiano acknowledge the support of the PRIN project "Mathematical and numerical modelling of the cardiovascular system, and their clinical applications". Gianluigi Rozza acknowledges the SISSA Excellence Grant NOFYSAS "Computational and Geometrical Reduction Strategies for the simulation, control and optimization of complex systems". We also acknowledge ERC Advanced Grant Mathcard (number 227058).

Appendix A. Additional details on the radial basis functions interpolation procedure

A.1. **Curve deformation of a single branch.** A radial basis functions (RBF) [49] interpolation is employed in the proposed framework to perform the deformation in step (B') from the reference curve $\boldsymbol{\gamma}(s)$ to the deformed one $\boldsymbol{\gamma}(s;\boldsymbol{\eta},\boldsymbol{\eta}')$, when dealing with the curve-based parametrization of a single vessel (Section 3.1). In particular, the deformed curve is obtained as follows:

$$\boldsymbol{\gamma}(s;\boldsymbol{\eta},\boldsymbol{\eta}') = \begin{bmatrix} W^T(\boldsymbol{\eta},\boldsymbol{\eta}') & U^T(\boldsymbol{\eta},\boldsymbol{\eta}') & \boldsymbol{c}(\boldsymbol{\eta},\boldsymbol{\eta}') & A(\boldsymbol{\eta},\boldsymbol{\eta}') \end{bmatrix} \begin{bmatrix} \boldsymbol{r}(s) \\ -\dot{\boldsymbol{r}}(s) \\ 1 \\ \boldsymbol{\gamma}(s) \end{bmatrix},$$

where the radial functions on the right-hand side are defined as

$$[\boldsymbol{r}(s)]_{i=1,\dots,N} = \sigma(\varepsilon\,|s-\mathfrak{s}_i|), \quad [\dot{\boldsymbol{r}}(s)]_{j=1,\dots,M} = \partial_s\sigma(\varepsilon\,|s-\mathfrak{r}_j|),$$

being $\varepsilon > 0$ a shape factor and $\sigma : \mathbb{R} \to \mathbb{R}$ a radial function such that $\sigma'(0) = 0$ (see Table 2 for some common radial functions). The unknown coefficients

$$W(\boldsymbol{\eta},\boldsymbol{\eta}') \in \mathbb{R}^{N\times 3}, \quad U(\boldsymbol{\eta},\boldsymbol{\eta}') \in \mathbb{R}^{M\times 3}, \quad \boldsymbol{c}(\boldsymbol{\eta},\boldsymbol{\eta}') \in \mathbb{R}^3, \quad A(\boldsymbol{\eta},\boldsymbol{\eta}') \in \mathbb{R}^{3\times 3}$$

Gaussian	$\sigma(r) = e^{-r^2}$
Inverse Multiquadric	$\sigma(r) = (1+r^2)^{-1/2}$
Multiquadric	$\sigma(r) = (1+r^2)^{1/2}$
Polyharmonic spline	$\sigma(r) = r^k$, k odd $\sigma(r) = r^k \log r$, k even
Wendland	$\sigma(r) = (1-r)_+^4(1+4r)$

Table 2. Some common functions $\sigma(r)$.

are obtained as the solution of the following symmetric linear system of small size $M+N+4$

$$\begin{bmatrix} R_{(0,0)} & R_{(0,1)} & \mathbf{1}_N & \Gamma \\ R_{(1,0)} & R_{(1,1)} & \mathbf{0}_M & T \\ \mathbf{1}_N^T & \mathbf{0}_M^T & 0 & \mathbf{0}_3^T \\ \Gamma^T & T^T & \mathbf{0}_3 & O_{3\times 3} \end{bmatrix} \begin{bmatrix} W(\boldsymbol{\eta},\boldsymbol{\eta}') \\ U(\boldsymbol{\eta},\boldsymbol{\eta}') \\ \boldsymbol{c}^T(\boldsymbol{\eta},\boldsymbol{\eta}') \\ A^T(\boldsymbol{\eta},\boldsymbol{\eta}') \end{bmatrix} = \begin{bmatrix} \Gamma + [\boldsymbol{\eta}] \\ T + [\boldsymbol{\eta}'] \\ \mathbf{0}_3^T \\ O_{3\times 3} \end{bmatrix} \tag{7}$$

being

$$\begin{aligned}
&\Gamma = [\boldsymbol{\gamma}(\mathfrak{s}_1)|\boldsymbol{\gamma}(\mathfrak{s}_2)|\dots|\boldsymbol{\gamma}(\mathfrak{s}_N)]^T \in \mathbb{R}^{N\times 3}, \qquad [\boldsymbol{\eta}] = [\boldsymbol{\eta}_1|\boldsymbol{\eta}_2|\dots|\boldsymbol{\eta}_N]^T \in \mathbb{R}^{N\times 3},\\
&T = [\boldsymbol{\gamma}'(\mathfrak{r}_1)|\boldsymbol{\gamma}'(\mathfrak{r}_2)|\dots|\boldsymbol{\gamma}'(\mathfrak{r}_M)]^T \in \mathbb{R}^{M\times 3}, \qquad [\boldsymbol{\eta}'] = [\boldsymbol{\eta}'_1|\boldsymbol{\eta}'_2|\dots|\boldsymbol{\eta}'_N]^T \in \mathbb{R}^{M\times 3},\\
&[R_{(0,0)}]_{i=1,\dots,N}^{I=1,\dots,N} = \sigma(\varepsilon\,|s-\mathfrak{s}_I|)|_{s=\mathfrak{s}_i}, \quad R_{(0,0)} \in \mathbb{R}^{N\times N},\\
&[R_{(0,1)}]_{i=1,\dots,N}^{J=1,\dots,M} = -\partial_s\sigma(\varepsilon\,|s-\mathfrak{r}_J|)|_{s=\mathfrak{s}_i}, \quad R_{(0,1)} \in \mathbb{R}^{N\times M},\\
&[R_{(1,0)}]_{j=1,\dots,M}^{I=1,\dots,N} = \partial_s\sigma(\varepsilon\,|s-\mathfrak{s}_I|)|_{s=\mathfrak{r}_j}, \quad R_{(1,0)} \in \mathbb{R}^{M\times N},\\
&[R_{(1,1)}]_{j=1,\dots,M}^{J=1,\dots,M} = -\partial_{ss}\sigma(\varepsilon\,|s-\mathfrak{r}_J|))|_{s=\mathfrak{r}_j}, \quad R_{(1,1)} \in \mathbb{R}^{M\times M}.
\end{aligned}$$

We recall that N is the number of points with prescribed displacement, while M is the number of points with prescribed tangent vector. Interpolation of parametrized displacements (derivatives, respectively) is a consequence of the first (second, resp.) line of (7), while the remaining lines are related to additional constraints to guarantee the uniqueness of the interpolation [49]. We remark that, in contrast to the standard approach in RBF interpolation, in our case we also interpolate the first derivative of the curve, in order to be able to impose a prescribed normal direction at anastomoses, as discussed in Section 3.2.

A.2. **Anastomosis deformation in a network.** Let us now turn to the case of anastomosis deformation in a network, as described in Section 3.2. Considering a similar approach as in A.1, once the displacement of the volume-based control points $\{\boldsymbol{p}_k\}_{k=1,\dots,L}$ is known, the deformed anastomosis is sought as [49, 50, 51]

$$\boldsymbol{V}(\boldsymbol{x};\boldsymbol{\eta},\boldsymbol{\eta}') = \begin{bmatrix} Y^T(\boldsymbol{\eta},\boldsymbol{\eta}') & \boldsymbol{f}(\boldsymbol{\eta},\boldsymbol{\eta}') & B(\boldsymbol{\eta},\boldsymbol{\eta}') \end{bmatrix} \begin{bmatrix} \boldsymbol{s}(\boldsymbol{x}) \\ 1 \\ \boldsymbol{x} \end{bmatrix}, \tag{8}$$

being

$$[\boldsymbol{s}(\boldsymbol{x})]_{k=1,\dots,L} = \sigma(\varepsilon\,\|\boldsymbol{x}-\boldsymbol{p}_l\|);$$

the unknown coefficients

$$Y(\boldsymbol{\eta},\boldsymbol{\eta}') \in \mathbb{R}^{L\times 3}, \quad \boldsymbol{f}(\boldsymbol{\eta},\boldsymbol{\eta}') \in \mathbb{R}^3, \quad B(\boldsymbol{\eta},\boldsymbol{\eta}') \in \mathbb{R}^{3\times 3}$$

are the solution of the following linear system

$$\begin{bmatrix} S & \mathbf{1}_L & P \\ \mathbf{1}_L^T & 0 & \mathbf{0}_3^T \\ P^T & \mathbf{0}_3 & O_{3\times 3} \end{bmatrix} \begin{bmatrix} Y(\boldsymbol{\eta},\boldsymbol{\eta}') \\ \boldsymbol{f}^T(\boldsymbol{\eta},\boldsymbol{\eta}') \\ B^T(\boldsymbol{\eta},\boldsymbol{\eta}') \end{bmatrix} = \begin{bmatrix} P + D(\boldsymbol{\eta},\boldsymbol{\eta}') \\ \mathbf{0}_3^T \\ O_{3\times 3} \end{bmatrix}$$

for

$$\begin{aligned}
&P = [\boldsymbol{p}_1|\boldsymbol{p}_2|\dots|\boldsymbol{p}_N]^T \in \mathbb{R}^{L\times 3}, \qquad D(\boldsymbol{\eta},\boldsymbol{\eta}') = [\boldsymbol{d}_1(\boldsymbol{\eta},\boldsymbol{\eta}')|\boldsymbol{d}_2(\boldsymbol{\eta},\boldsymbol{\eta}')|\dots|\boldsymbol{d}_L(\boldsymbol{\eta},\boldsymbol{\eta}')]^T \in \mathbb{R}^{L\times 3},\\
&[S]_{k=1,\dots,L}^{K=1,\dots,L} = \sigma(\varepsilon\,\|\boldsymbol{x}-\boldsymbol{p}_K\|)|_{\boldsymbol{x}=\boldsymbol{p}_k}, \quad S \in \mathbb{R}^{L\times L}.
\end{aligned}$$

where L is the number of control points and $\boldsymbol{d}_l(\boldsymbol{\eta},\boldsymbol{\eta}')$, $l=1,\dots,L$, are known displacements (e.g. computed employing the curved based approach for control points on the interface). Two suggestions for the choice of control points, to guarantee both continuity at the interface with other branches and smoothness near the anastomosis, have been discussed in Section 3.2.

References

References

[1] J. W. Kirklin, B. G. Barratt-Boyes, Cardiac surgery: morphology, diagnostic criteria, natural history, techniques, results, and indications, Churchill Livingstone New York, 1988.

[2] J. W. Butany, T. E. David, M. Ojha, Histological and morphometric analyses of early and late aortocoronary vein grafts and distal anastomoses, The Canadian Journal of Cardiology 14 (5) (1998) 671–677.

[3] H. S. Bassiouny, S. White, S. Glagov, E. Choi, D. P. Giddens, C. K. Zarins, Anastomotic intimal hyperplasia: mechanical injury or flow induced, Journal of Vascular Surgery 15 (4) (1992) 708–717.

[4] M. Hofer, G. Rappitsch, K. Perktold, W. Trubel, H. Schima, Numerical study of wall mechanics and fluid dynamics in end-to-side anastomoses and correlation to intimal hyperplasia, Journal of Biomechanics 29 (10) (1996) 1297–1308.

[5] N. Staalsen, M. Ulrich, J. Winther, E. M. Pedersen, T. How, H. Nygaard, The anastomosis angle does change the flow fields at vascular end-to-side anastomoses in vivo, Journal of Vascular Surgery 21 (3) (1995) 460–471.

[6] F. Loth, P. F. Fischer, H. S. Bassiouny, Blood flow in end-to-side anastomoses, Annual Review of Fluid Mechanics 40 (2008) 367–393.

[7] C. A. Taylor, M. T. Draney, Experimental and computational methods in cardiovascular fluid mechanics, Annual Review of Fluid Mechanics 36 (2004) 197–231.

[8] L. Formaggia, A. Quarteroni, A. Veneziani, Cardiovascular mathematics: modeling and simulation of the circulatory system, Vol. 1 of MS&A series, Springer-Verlag Italia, 2009.

[9] A. Quarteroni, G. Rozza (Eds.), Reduced Order Methods for Modeling and Computational Reduction, Vol. 9, Springer, MS&A Series, 2014.

[10] A. Quarteroni, G. Rozza, Optimal control and shape optimization of aorto-coronaric bypass anastomoses, Mathematical Models and Methods in Applied Sciences 13 (12) (2003) 1801–1824.

[11] G. Rozza, Shape design by optimal flow control and reduced basis techniques: applications to bypass configurations in haemodynamics, Ph.D. thesis, École Polytechnique Fédérale de Lausanne, N. 3400 (2005).

[12] G. Rozza, On optimization, control and shape design of an arterial bypass, International Journal for Numerical Methods in Fluids 47 (10-11) (2005) 1411–1419.

[13] V. Agoshkov, A. Quarteroni, G. Rozza, A mathematical approach in the design of arterial bypass using unsteady Stokes equations, Journal of Scientific Computing 28 (2006) 139–165.

[14] V. Agoshkov, A. Quarteroni, G. Rozza, Shape design in aorto-coronaric bypass anastomoses using perturbation theory, SIAM Journal On Numerical Analysis 44 (1) (2007) 367–384.

[15] A. Manzoni, A. Quarteroni, G. Rozza, Shape optimization for viscous flows by reduced basis methods and free-form deformation, International Journal for Numerical Methods in Fluids 70 (5) (2012) 646–670.

[16] T. Lassila, A. Manzoni, A. Quarteroni, G. Rozza, Boundary control and shape optimization for the robust design of bypass anastomoses under uncertainty, ESAIM: Mathematical Modelling and Numerical Analysis 47 (4) (2013) 1107–1131.

[17] K. McLeod, A. Caiazzo, M. Fernández, T. Mansi, I. Vignon-Clementel, M. Sermesant, X. Pennec, Y. Boudjemline, J.-F. Gerbeau, Atlas-based reduced models of blood flows for fast patient-specific simulations, in: O. Camara, M. Pop, K. Rhode, M. Sermesant, N. Smith, A. Young (Eds.), Statistical Atlases and Computational Models of the Heart, Vol. 6364 of Lecture Notes in Computer Science, Springer Berlin / Heidelberg, 2010, pp. 95–104.

[18] R. Guibert, K. McLeod, A. Caiazzo, T. Mansi, M. A. Fernández, M. Sermesant, X. Pennec, I. E. Vignon-Clementel, Y. Boudjemline, J.-F. Gerbeau, Group-wise construction of reduced models for understanding and characterization of pulmonary blood flows from medical images, Medical Image Analysis 18 (1) (2014) 63–82.

[19] D. Ghista, F. Kabinejadian, Coronary artery bypass grafting hemodynamics and anastomosis design: a biomedical engineering review, BioMedical Engineering OnLine 12 (1) (2013) 129:1–129:28.

[20] F. Migliavacca, G. Dubini, Computational modeling of vascular anastomoses, Biomechanics and Modeling in Mechanobiology 3 (4) (2005) 235–250.

[21] A. L. Marsden, Optimization in cardiovascular modeling, Annual Review of Fluid Mechanics 46 (1) (2014) 519–546.

[22] A. A. Owida, H. Do, Y. S. Morsi, Numerical analysis of coronary artery bypass grafts: an over view, Computer Methods and Programs in Biomedicine 108 (2) (2012) 689–705.

[23] F. Ballarin, A. Manzoni, A. Quarteroni, G. Rozza, Supremizer stabilization of POD–Galerkin approximation of parametrized steady incompressible Navier–Stokes equations, International Journal for Numerical Methods in Engineering 102 (5) (2015) 1136–1161.

[24] L. Antiga, M. Piccinelli, L. Botti, B. Ene-Iordache, A. Remuzzi, D. Steinman, An image-based modeling framework for patient-specific computational hemodynamics, Medical and Biological Engineering and Computing 46 (2008) 1097–1112.

[25] A. Fedorov, R. Beichel, J. Kalpathy-Cramer, J. Finet, J.-C. Fillion-Robin, S. Pujol, C. Bauer, D. Jennings, F. Fennessy, M. Sonka, J. Buatti, S. Aylward, J. V. Miller, S. Pieper, R. Kikinis, 3D Slicer as an image computing platform for the quantitative imaging network, Magnetic Resonance Imaging 30 (9) (2012) 1323–1341.

[26] F. Ballarin, Reduced-order models for patient-specific haemodynamics of coronary artery bypass grafts, Ph.D. thesis, Department of Mathematics, Politecnico di Milano, `http://hdl.handle.net/10589/102804` (2015).

[27] L. Antiga, Patient-specific modeling of geometry and blood flow in large arteries, Ph.D. thesis, Dipartimento di Bioingegneria, Politecnico di Milano (2002).

[28] M. Piccinelli, A. Veneziani, D. A. Steinman, A. Remuzzi, L. Antiga, A framework for geometric analysis of vascular structures: application to cerebral aneurysms, IEEE Transactions on Medical Imaging 28 (8) (2009) 1141–1155.

[29] F. Lazarus, S. Coquillart, P. Jancène, Interactive axial deformations, in: Modeling in Computer Graphics, Springer-Verlag, 1993, pp. 241–254.

[30] I. Llamas, A. Powell, J. Rossignac, C. D. Shaw, Bender: a virtual ribbon for deforming 3D shapes in biomedical and styling applications, in: Proceedings of the 2005 ACM symposium on solid and physical modeling, 2005, pp. 89–99.

[31] S.-H. Yoon, M.-S. Kim, Sweep-based freeform deformations, Computer Graphics Forum 25 (3) (2006) 487–496.

[32] L. Antiga, D. A. Steinman, Robust and objective decomposition and mapping of bifurcating vessels, IEEE Transactions on Medical Imaging 23 (6) (2004) 704–713.

[33] I. A. Kakadiaris, A. Santamaria-Pang, A. Pednekar, Functional morphology analysis of the left anterior descending coronary artery in EBCT images, IEEE Transactions on Biomedical Engineering 57 (8) (2010) 1886–1896.

[34] R. L. Bishop, There is more than one way to frame a curve, American Mathematical Monthly 82 (3) (1975) 246–251.

[35] A. J. Hanson, H. Ma, Parallel transport approach to curve framing, Technical report TR425, Indiana University (1995).

[36] D. Fei, J. D. Thomas, S. E. Rittgers, The effect of angle and flow rate upon hemodynamics in distal vascular graft anastomoses: a numerical model study, Journal of Biomechanical Engineering 116 (3) (1994) 331–336.

[37] J. Baiges, R. Codina, S. Idelsohn, Explicit reduced-order models for the stabilized finite element approximation of the incompressible Navier–Stokes equations, International Journal for Numerical Methods in Fluids 72 (12) (2013) 1219–1243.

[38] J. Burkardt, M. Gunzburger, H.-C. Lee, POD and CVT-based reduced-order modeling of Navier–Stokes flows, Computer Methods in Applied Mechanics and Engineering 196 (1–3) (2006) 337–355.

[39] Z. Luo, J. Chen, I. Navon, X. Yang, Mixed finite element formulation and error estimates based on Proper Orthogonal Decomposition for the nonstationary Navier–Stokes equations, SIAM Journal on Numerical Analysis 47 (1) (2009) 1–19.

[40] A. Manzoni, An efficient computational framework for reduced basis approximation and a posteriori error estimation of parametrized Navier–Stokes flows, ESAIM: Mathematical Modelling and Numerical Analysis 48 (2014) 1199–1226.

[41] G. Rozza, D. B. P. Huynh, A. Manzoni, Reduced basis approximation and a posteriori error estimation for Stokes flows in parametrized geometries: roles of the inf-sup stability constants, Numerische Mathematik 125 (1) (2013) 115–152.

[42] G. Rozza, K. Veroy, On the stability of the reduced basis method for Stokes equations in parametrized domains, Computer Methods in Applied Mechanics and Engineering 196 (7) (2007) 1244–1260.

[43] M. Barrault, Y. Maday, N. C. Nguyen, A. T. Patera, An 'empirical interpolation' method: application to efficient reduced-basis discretization of partial differential equations, Comptes Rendus Mathematique 339 (9) (2004) 667–672.

[44] J. Keegan, P. D. Gatehouse, G.-Z. Yang, D. N. Firmin, Spiral phase velocity mapping of left and right coronary artery blood flow: correction for through-plane motion using selective fat-only excitation, Journal of Magnetic Resonance Imaging 20 (6) (2004) 953–960.

[45] N. Ishida, H. Sakuma, B. P. Cruz, T. Shimono, T. Tokui, I. Yada, K. Takeda, C. B. Higgins, MR flow measurement in the internal mammary artery–to–coronary artery bypass graft: comparison with graft stenosis at radiographic angiography, Radiology 220 (2) (2001) 441–447.

[46] F. Ballarin, E. Faggiano, S. Ippolito, A. Manzoni, A. Quarteroni, G. Rozza, R. Scrofani, A fast computational framework for haemodynamics of coronary artery bypass grafts: application to several patient-specific cases, submitted.

[47] D. J. Knezevic, J. W. Peterson, A high-performance parallel implementation of the certified reduced basis method, Computer Methods in Applied Mechanics and Engineering 200 (13–16) (2011) 1455–1466.

[48] B. S. Kirk, J. W. Peterson, R. H. Stogner, G. F. Carey, libMesh: a C++ library for parallel adaptive mesh refinement/coarsening simulations, Engineering with Computers 22 (3-4) (2006) 237–254.

[49] M. D. Buhmann, Radial Basis Functions: theory and implementations, Cambridge University Press, 2003.
[50] A. Manzoni, A. Quarteroni, G. Rozza, Model reduction techniques for fast blood flow simulation in parametrized geometries, International Journal for Numerical Methods in Biomedical Engineering 28(6–7) (2012) 604–625.
[51] D. Forti, G. Rozza, Efficient geometrical parametrisation techniques of interfaces for reduced-order modelling: application to fluid–structure interaction coupling problems, International Journal of Computational Fluid Dynamics 28 (3-4) (2014) 158–169.

MOX Technical Reports, last issues

Dipartimento di Matematica
Politecnico di Milano, Via Bonardi 9 - 20133 Milano (Italy)

50/2015 Grillo, A.; Guaily, A.; Giverso, C.; Federico, S.
Non-Linear Model for Compression Tests on Articular Cartilage

49/2015 Ghiglietti, A.; Ieva, F.; Paganoni, A.M.
Statistical inference for stochastic processes: two sample hypothesis tests

48/2015 Ambrosi, D.; Pettinati, V.; Ciarletta, P.
Active stress as a local regulator of global size in morphogenesis

47/2015 Colombo, M. C.; Giverso, C.; Faggiano, E.; Boffano,C.; Acerbi, F.; Ciarletta, P.
Towards the personalized treatment of glioblastoma: integrating patient-specific clinical data in a continuous mechanical model

45/2015 Lange, M.; Palamara, S.; Lassila, T.; Vergara, C.; Quarteroni, A.; Frangi, A.F.
Improved hybrid/GPU algorithm for solving cardiac electrophysiology problems on Purkinje networks

46/2015 Giverso, C.; Verani, M.; Ciarletta P.
Emerging morphologies in round bacterial colonies: comparing volumetric versus chemotactic expansion

44/2015 Antonietti, P.F.; Houston, P.; Smears, I.
A note on optimal spectral bounds for nonoverlapping domain decomposition preconditioners for hp-Version Discontinuous Galerkin methods

43/2015 Deparis, S.; Forti, D.; Gervasio, P.; Quarteroni, A.
INTERNODES: an accurate interpolation-based method for coupling the Galerkin solutions of PDEs on subdomains featuring non-conforming interfaces

42/2015 Brugiapaglia, S.; Nobile, F.; Micheletti, S.; Perotto, S.
A theoretical study of COmpRessed SolvING for advection-diffusion-reaction problems

41/2015 Quarteroni, A.; Veneziani, A.; Vergara, C.
Geometric multiscale modeling of the cardiovascular system, between theory and practice